POLYMER-INDUCED TURBULENCE MODIFICATIONS IN AN IMPINGING JET

BY

RICARDO MEJIA ALVAREZ

THESIS

Submitted in partial fulfillment of the requirements
for the degree of Master of Science in Theoretical and Applied Mechanics
in the Graduate College of the
University of Illinois at Urbana-Champaign, 2010

Urbana, Illinois

Adviser:

Associate Professor Kenneth T. Christensen

Abstract

This effort explores the impact of dilute polymer solutions on the turbulence characteristics in a submersed liquid impinging-jet configuration. Turbulent impinging jets are commonly used in technological applications such as drying, scouring, cooling or heating due to an enhancement in transport characteristics in the impingement region under certain nozzle-to-wall configurations. Previous efforts have identified significant turbulence modifications in the presence of dilute concentrations of polymer (i.e., the Toms effect) in both bounded (suppression) and unbounded (either suppression or enhancement) flows. To this end, particle-image velocimetry measurements were made for an axisymmetric turbulent impinging jet with a nozzle-to-wall distance $H/D = 6.8$ and Reynolds number $\mathrm{Re}_D = 23000$. Measurements were made for both plain water and dilute polymer solutions of polyethylene oxide at concentrations of 50 and 100 ppm. The mean and turbulence characteristics of these three flows are contrasted and it is observed that the 50 ppm case yields a slight enhancement of the turbulence while the 100 ppm case exhibits clear suppression of the turbulence.

Acknowledgments

I want to thank my advisor, Professor Kenneth Christensen, for supervising my work. Thanks to his guidance and understanding during the time I carried out this project, I was able to master PIV and several data analysis tools which are instrumental for experimental research in fluid dynamics.

This work was funded by the University of Illinois.

Table of Contents

List of Figures

Chapter 1

Introduction

The interaction between a turbulent free jet and the fluid surrounding it is characterized by the onset of spatial instabilities that give rise to large-scale coherent structures such as ring or spiral vortices. In turn, these structures control the overall configuration of the jet as they develop while advecting downstream. In other words, the degree of development of large-scale coherent structures in a free jet correlates with their distance from the nozzle. With increasing distance, these structures themselves can become unstable leading to the possibility of vortex pairing as well as vortex annihilation which gives rise to a wide range of smaller turbulent scales.

Given this free-jet development scenario, when such a jet impinges a surface the level of interaction between the jet and the wall is strongly dependent upon the nozzle-to-wall distance (H) relative to the exit diameter of the jet nozzle (D). In other words, the detailed physics of this interaction are intimately tied to the degree of development of the large-scale structures of the jet. Indeed, impinging-jet configurations occur in a wide variety of technologically-relevant applications, including cooling, heating and drying operations, drilling, cutting, mixing and fire-fighting. Many of these applications rely upon the high heat-transfer rates achievable in the stagnation region near the surface as well as the intense straining generated by this flow configuration (Goldstein and Franchett, 1988; Baughn and Shimizu, 1989; Jambunathan et al., 1992; Sakakibara et al., 1996, among many others). On a more fundamental note, impinging jets have received considerable attention from a basic research standpoint because they contain many flow features necessary for proper validation of turbulence models, including free-shear and near-wall regions and zones of intense streamline curvature (Fairweather and Hargrave, 2002, for example).

This chapter provides a detailed background on the structural aspects of turbulent free jets as a prelude to a discussion of the complex interactions that occur when such a jet abruptly impinges a surface. The results of a few previous studies regarding the impact of dilute polymer solutions

on both of these jet configurations is then introduced as motivation for the present experimental effort.

1.1 Structure of Free Jets

Figure 1.1 presents a schematic of both the instantaneous and time-average structure of a turbulent free jet. Following Browand and Laufer (1977) and List (1982), two dominant modes are recognized in free jets: axisymmetric and azimuthal. The first is characterized by the presence of ring vortices (figure 1.1a), and the second by a single spiral vortex (figure 1.1b). For both of these modes, it is possible to distinguish four main regions in turbulent free jets: the near region, the puffing region, the developing region and the self-similar region.

The near region of a free jet is that in which the potential core is still present, whose length is typically $5 - 8D$ (see figure 1.1). Note that the boundary of the potential core is typically defined by the locations at which the velocity is 95% of the centerline velocity at the nozzle exit (U_e). This region is in turn composed of two sub-regions: the straining region and the interacting region. The straining region begins at the exit of the jet, extends typically no more than one diameter, and is characterized by an unstable laminar shear layer accompanied by strong velocity gradients (Browand and Laufer, 1977). Subsequently, the interacting region extends from the end of the straining region to the tip of the potential core. In this region, for Reynolds numbers ($\mathrm{Re} \equiv U_e D/\nu$, where ν is the kinematic viscosity of the fluid) in the range $5000 < \mathrm{Re}_D < 10000$, ring vortices generated by means of instabilities in the straining region grow and interact with one another via a pairing mechanism (Browand and Laufer, 1977). The larger vortex resulting from pairing grows in size while its vorticity propagates radially inward until reaching the axis of the jet at $x/D \approx 5$. At this location, the vortex core disappears to mark the end of the near region and the beginning of the puffing region. For $10000 < \mathrm{Re}_D < 15000$, the azimuthal mode begins to influence the vortices, as they show from four to nine lobes and may become azimuthally-wavy rings (Citriniti and George, 2000; Ganapathisubramani et al., 2002). The interaction between them follows the same process described above. At $\mathrm{Re}_D \geq 15000$, the flow appears dominated by the azimuthal mode as the ring vortices give way to a single helical vortex for about 50% of the time (Browand and Laufer, 1977). Even though the interaction in the helical mode is quite different, the flow still

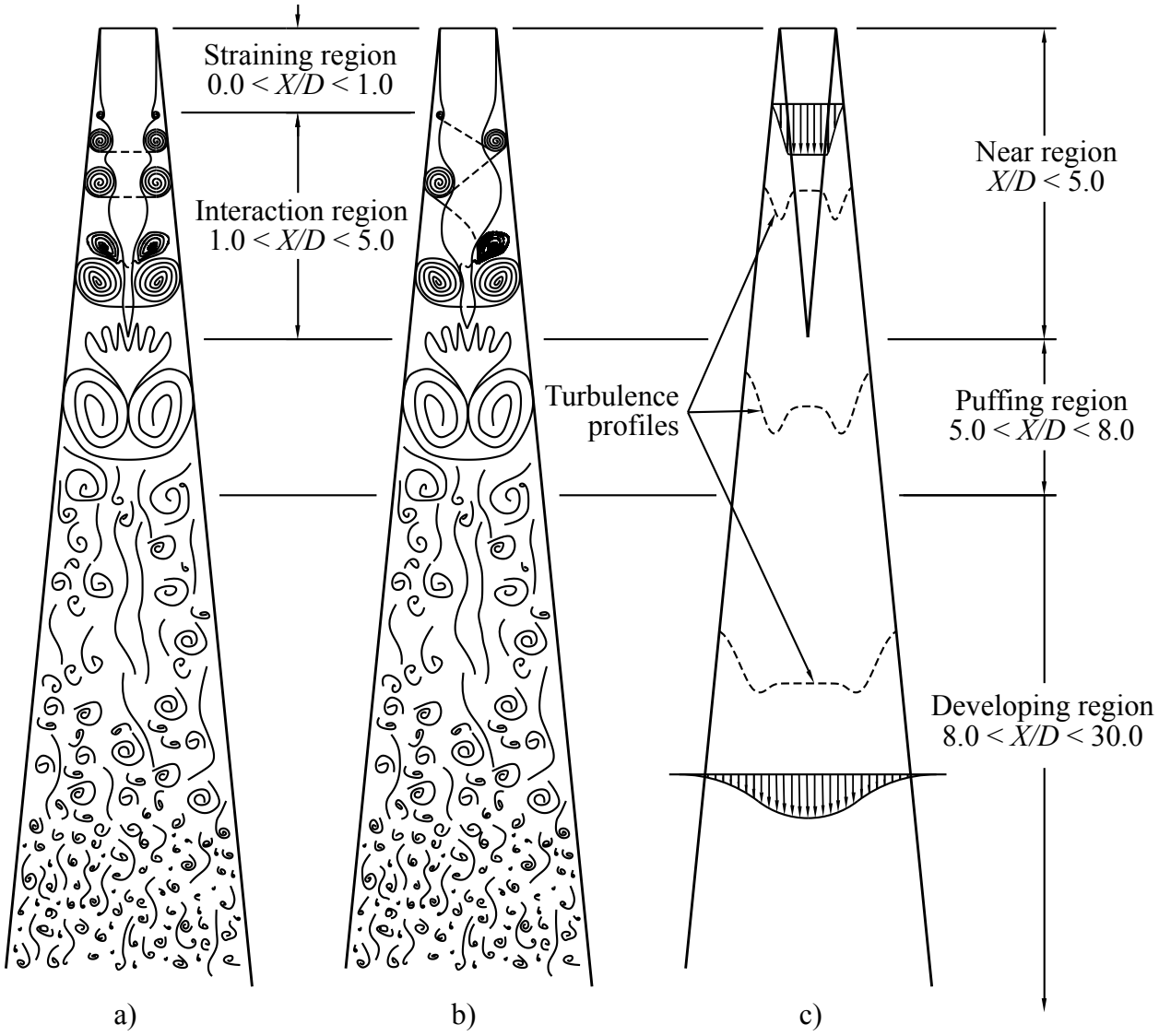

Figure 1.1: Structure of a free jet. a) Axisymmetric mode, $1000 < \mathrm{Re}_D < 15000$; b) Azimuthal mode, $\mathrm{Re}_D > 15000$; c) Ensemble average of a turbulent jet.

shows a marked tendency to form ring-like structures. In particular, adjacent parts of the helical vortex tend to get close to each other so that the pitch of the helix tends to zero near the end of the potential core (Browand and Laufer, 1977). In consequence, a pairing of adjacent quasi-rings forms, resulting in the same outcome of the axisymmetric mode wherein the core of a large ring vortex grows in diameter until reaching the axis of the jet. Again, at $x/D \approx 5$, this core disappears to mark the end of the near region and the beginning of the puffing region (Browand and Laufer, 1977).

Interestingly, the radial profile of streamwise velocity becomes gradually bell-shaped as the jet spreads radially at a linear rate (Fitzgerald and Garimella, 1998). Even though it reaches a bell shape at the end of the interacting region, it has not yet reached a self-similar state (Corrsin, 1943; Corrsin and Kistler, 1955; Fitzgerald and Garimella, 1998). The radial spread of the jet results from the growth of the mixing layer, which in turn can be related to the growth of ring- or spiral-like coherent structures (Browand and Laufer, 1977; List, 1982). In consequence, for a given axial position within the interacting region, the radial distribution of turbulence intensity peaks at the center of the mixing layer, exhibiting an annular maximum at $r/D \approx 0.5$ (Corrsin, 1943; Corrsin and Kistler, 1955; Angioletti et al., 2003; Gardon and Cobonpue, 1962; Gardon and Akfirat, 1965; Fitzgerald and Garimella, 1998). At the same time, the turbulence intensity increases monotonically along the axial coordinate in the interacting region as the jet broadens radially (Barker, 1973; Vlasov et al., 1973). Another interesting point to note is that, keeping other exit conditions of the jet fixed, the length of the potential core appears to be independent of Re_D. In consequence, since the radial spreading of axisymmetric turbulent jets is linear, the time-averaged structure of the near-jet region would be independent of Reynolds number.

The puffing region is typically located in the interval $5.0 < x/D < 8.0$ (see figure 1.1). In this region, the ring vortices have already paired and spread radially inward to the jet centerline. The paired structure degenerates into a puff, produces additional turbulence, and starts a breakdown process toward classical cascading (Browand and Laufer, 1977). The turbulence intensity along the center line reaches its maximum at the end of the puffing region, beyond which it begins to decrease. The velocity profile is still bell-shaped but non self-similar, and the radial profile of turbulence intensity is still bi-modal (Corrsin, 1943; Corrsin and Kistler, 1955).

The developing region is that in which both the velocity and turbulence intensity profiles develop self-similarity (see figure 1.1). Such a development takes place as the turbulent kinetic energy (TKE) spreads radially as the jet grows in cross-section. The developing region occurs typically in the interval $8.0 < x/D < 30.0$. The radial profile of turbulence intensity becomes bell-shaped in the interval $10.0 < x/D < 20.0$, but one must approach $x/D \approx 30.0$ before a self-similar state is reached (Corrsin, 1943; Corrsin and Kistler, 1955; Barker, 1973; Vlasov et al., 1973). Beyond this distance, the jet is in a self-similar state wherein both the turbulence intensity and mean velocity

profiles decay in a self-similar manner (i.e., their decay can be reconciled with the growth of the jet cross-section with increasing x).

1.2 Structure of Impinging Jets

The average structure of a turbulent impinging jet is depicted in figure 1.2. Depending upon the nozzle-to-wall distance, two main impinging jet configurations might be observed: $H < L$ and $H > L$, where L is the length of the potential core in the absence of impingement surface. For these two impinging-jet configurations, three main regions can be distinguished: the free jet region, the impingement region and the wall jet region. The free jet region extends from the exit of the nozzle to approximately $1.2D$ from the surface. In this region, the jet conserves the same characteristics of a turbulent free jet as described above.

The impingement region is defined as the region where the jet is deflected by the impingement surface. Due to this deflection, the impingement region is marked by a radial favorable pressure gradient which, in turn, leads to stabilization of a very thin laminar boundary layer. The structure of this boundary layer depends strongly on the nozzle-to-wall configuration. As can be seen in figure 1.2b, when the nozzle-to-wall distance is shorter than the length of the potential core ($H < L$), the laminar boundary layer in the impingement region is directly influenced by the ring-like coherent structures generated within the mixing layer of the free jet. As a result, its thickness is minimum in an annular region of radius $r/D \approx 0.5$ (labeled 'A' in figure 1.2b), which is were ring-like structures reach the wall (Kezios, 1956; Angioletti et al., 2003). Moreover, the transport of passive scalars is maximum in this annular region regardless of the Reynolds number (Gardon and Akfirat, 1965). Additionally, this annular peak for the transport of passive scalars coincides with that of the turbulence intensity within the mixing layer of the free jet region (§ 1.1). In other words, previous experimental observations suggest that the transport of passive scalars in the annular region $r/D \approx 0.5$ is strongly correlated with the turbulence intensity generated in the mixing layer of the free jet by means of ring-like coherent structures [reference]. On the other hand, as can be seen in figure 1.2a, when the nozzle-to-wall distance is longer than the length of the potential core ($H > L$), the annular minimum of the thickness of the boundary layer in the impingement region disappears. As a consequence, the laminar boundary layer stabilized within the impingement

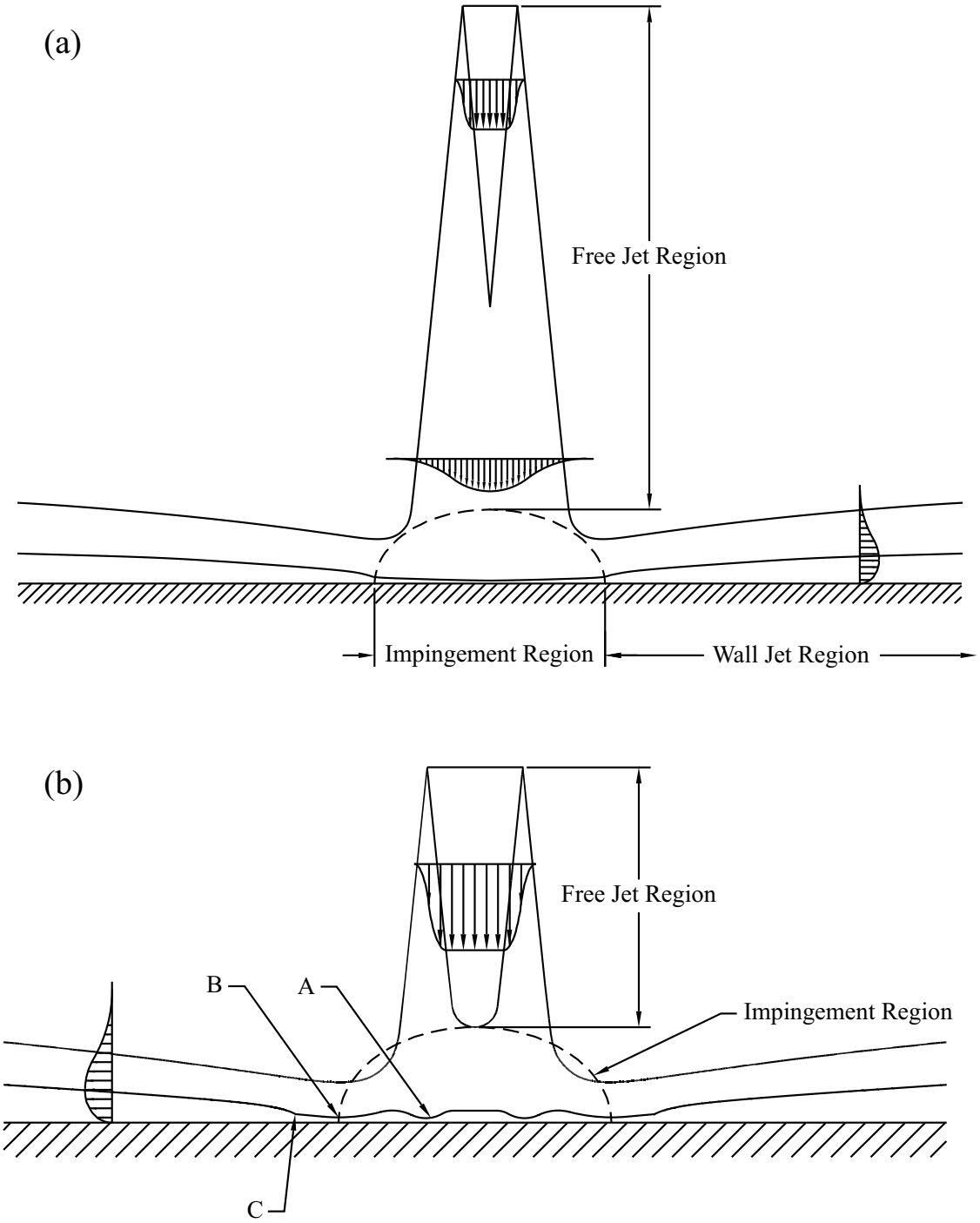

Figure 1.2: Structure of an impinging jet. a) $H > L$, the boundary layer grows up continuously. b) $H < L$, for intermediate Reynolds numbers, the boundary layer has two annular dimples, one at $r/D = 0.5$ (labeled 'A') and another at the end of the impingement region ($r/D \approx 1.0$, labeled 'B'), and presents a transition to turbulence whose radial location depends on the Reynolds number (labeled 'C').

region grows continuously along the radial coordinate. Therefore, the radial profiles of turbulence intensity and transport coefficients peak in the stagnation point and become bell-shaped (Gardon and Cobonpue, 1962; Gardon and Akfirat, 1965). Nevertheless, regardless of the nozzle-to-wall distance and the Reynolds number, the radial position at which the radial velocity and shear stress reach maximum remains $r/D \approx 1.0$. This radial position is considered to be the end of the impingement region and thus the beginning of the wall-jet region (Fitzgerald and Garimella, 1998; Koziol and Glowacki, 1989; Glowacki, 1989).

These statistical features of the impingement region have been linked to complex vortex interactions in the immediate vicinity of the surface. Such observations were first reported by Harvey and Perry (1971) who observed separation of the flow along the wall downstream of the stagnation point and the accompanied formation of secondary structures. These secondary structures appeared to form downstream of primary vortices that originated in the free-jet region. Such observations are consistent with the body of work associated with the surface impingement of isolated vortex rings (Walker et al., 1987, for example). The particle-image velocimetry (PIV) measurements of Landreth and Adrian (1990) provide detailed instantaneous views of the vortex interactions in a turbulent circular impinging jet for $H/D = 4$ where secondary structures are observed downstream and below primary vortices. The formation location of these secondary vortices was approximately two diameters downstream of the jet centerline and was accompanied by local flow separation. Further downstream, the thickness of the wall jet was observed to increase dramatically. In addition, the secondary vortices were found to quickly break away from the near-wall region before being advected downstream. Similar observations were reported by Sakakibara et al. (1996) for a two-dimensional turbulent jet. These complex vortical interactions appear to be relatively insensitive to H/D as Maurel and Solliec (2001) observed such behavior for nozzle-to-plate spacings as large as $50D$.

Finally, the wall jet region is that in which the jet spreads radially outward along the impingement surface. As was already mentioned, it starts at $r/D \approx 1.0$, where the mean radial velocity and shear stress reach maxima. For configurations in which $H/D > L$, the radial distribution of transport coefficients decreases continuously as the jet spreads radially, following up the bell-shape they take in the impingement region. In this case, the Reynolds number and the nozzle-to-wall dis-

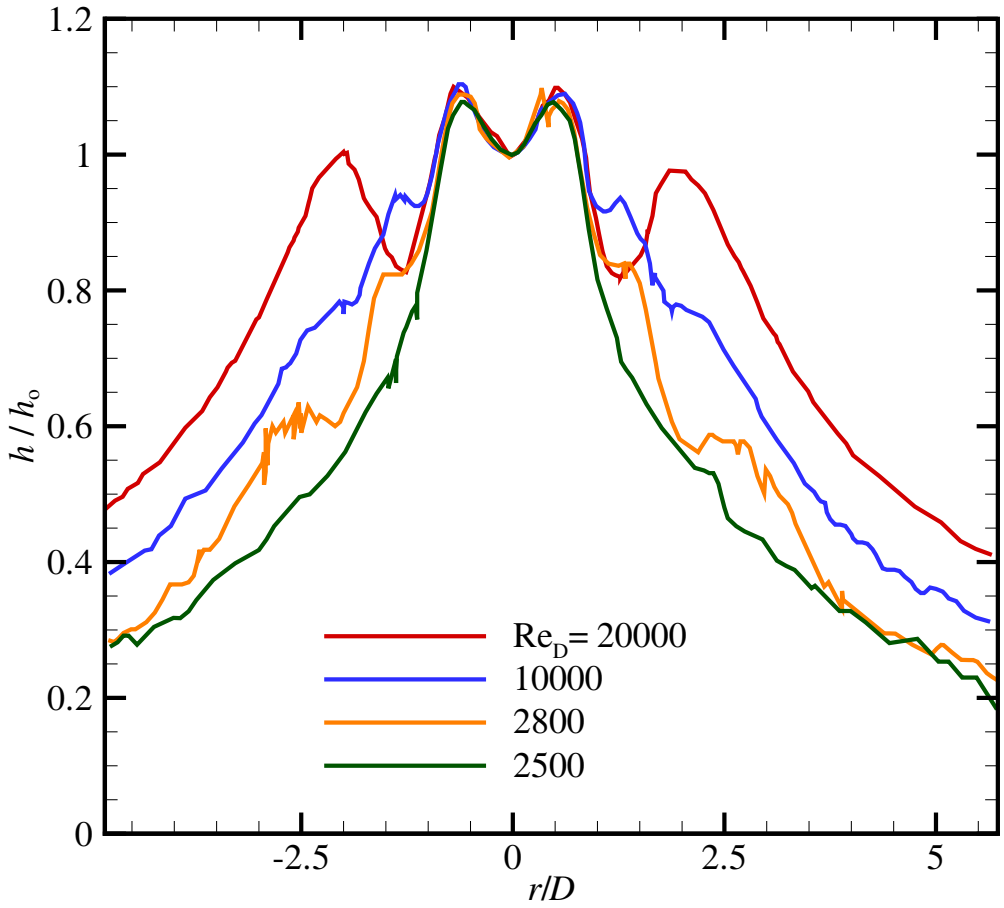

Figure 1.3: Influence of Reynolds number on the radial profiles of heat transfer for an axisymmetric impinging jet. $H/D = 2.0$. Source: Gardon and Akfirat (1965).

tance affect the magnitude of the transport coefficients without distorting their radial distribution significantly (Baughn and Shimizu, 1989; Angioletti et al., 2003).

Of particular interest is understanding how the complex kinematic features of impinging jet flows are related to observations of enhanced heat transfer in the impingement region. Early work by (Gardon and Cobonpue, 1962), and (Gardon and Akfirat, 1965) indicate that maximum stagnation-point heat transfer occurs for nozzle-to-wall distances in the range $6.0 < H/D < 7.0$. Moreover, Schlunder and Gnielinski (1967) found that the maximum axial turbulence intensity and maximum stagnation-point heat transfer occur for $H/D = 7.5$. As such, heat transfer in the stagnation region is highly dependent upon H/D as well as the nozzle geometry, the Reynolds number, etc. (Jambunathan et al., 1992). Several efforts have also shown that the Nusselt number

(Nu) has local maxima at multiple locations away from the jet centerline, most notably for $H/D < 6$ (Gardon and Cobonpue, 1962; Popiel and Boguslawski, 1988; Baughn and Shimizu, 1989) as illustrated in figure 1.3. In particular, Gardon and Cobonpue (1962) observed three distinct maxima (at radial locations $r/D = 0.5$, 1.5 and 2.5) for lower Reynolds numbers and two distinct maxima (at $r/D = 0.5$ and 2) at higher Reynolds numbers. The latter observation is consistent with the results of Baughn and Shimizu (1989) which revealed two peaks in Nu for $H/D = 2$ and also found the maximum stagnation-point Nu to occur for $H/D = 6$. Interestingly, the radial location of the second local maximum in Nu is consistent with the location where secondary vortical structures are observed to form and lift from the surface (Landreth and Adrian, 1990; Sakakibara et al., 1996). In particular, the simultaneous velocity and temperature measurements of Sakakibara et al. (1996) revealed counter-rotating pairs of vortices in a plane impinging jet that consistently drew hot fluid from the wall and ejected it into the outer flow while sweeping cooler fluid from the outer region towards the hotter wall. Therefore, the complex vortex interactions that exist in the impingement region appear to play a defining role in the enhanced heat transfer often observed near the impingement surface. In this regard, if these structures can somehow be intensified in nature (i.e., enhancement of turbulence in the impingement region), a commensurate enhancement of heat transfer may be achieved as well.

1.3 Polymer Effects

While the kinematic and heat-transfer characteristics of impinging jet flows are fairly well understood, the addition of a small amount of polymer generates flows that are quite distinct from Newtonian flows even at similar Reynolds numbers. Figure 1.4 presents three dye visualizations of free jets adapted from Berman and Tan (1985). The first image is of a water jet and displays the characteristic spreading and range of scales consistent with a free turbulent jet. However, when a small amount (100 ppm) of PEO is added to this flow (figure 1.4b) the spatial characteristics are dramatically altered, including some suppression of the primary vortices as well as small-scale turbulence along with a much weaker downstream growth rate. Different polymers and solvent conditions can yield quite distinct results as addition of 100 ppm of PAM in deionized water (figure 1.4c) further suppresses the growth of the primary vortices and the radial growth of the jet.

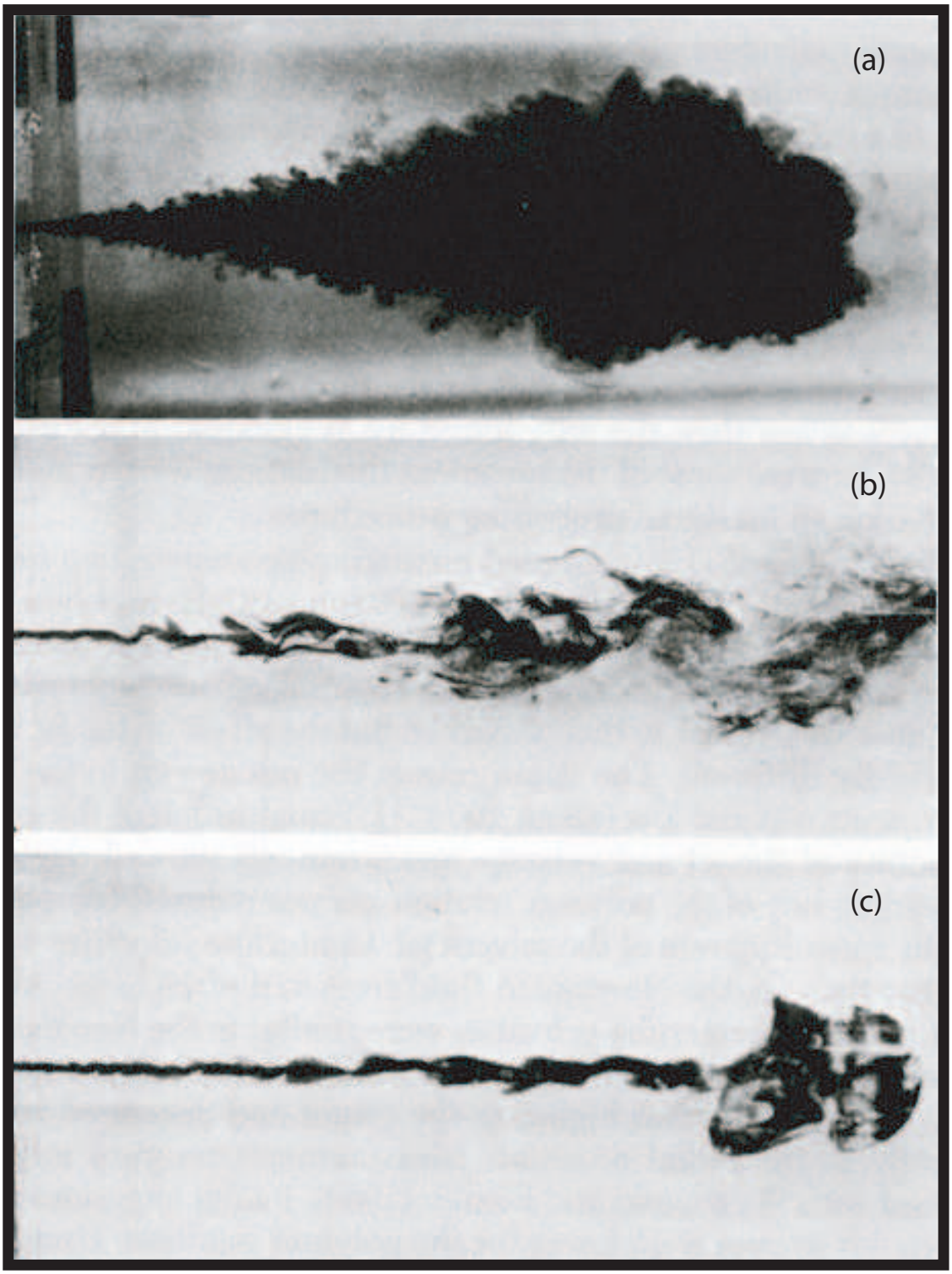

Figure 1.4: Examples of turbulence modifications in free jets due to polymer additives. a) Water; b) 100 ppm PEO in distilled water; c) 100 ppm PAM in deionized water [Adapted from Berman and Tan (1985)].

The latter two jets are in fact reminiscent of laminar free jets, indicating that the polymer generates a stabilizing effect that delays the transition to turbulence. Similar observations were reported by Hoyt et al. (1974).

Quantitative measurements of polymer jets, both free and impinging, show wide scatter with regard to the influence of the polymer. Barker (1973) observed that polymer additives (50 and 100 ppm) in a free jet issuing from a converging nozzle with no upstream development length had little influence on the mean axial velocity and turbulence intensity. In contrast, Barker observed jets issuing from pipes with long development lengths to have larger axial turbulence intensities and faster spreading rates. These observations are somewhat counter to those of Usui and Sano (1980) who found similar polymer additions to reduce the spreading rate of a free jet while generating higher values of the axial turbulence intensity that decayed more rapidly with radial position. They also observed reduced values of the radial turbulence intensity and Reynolds shear stresses with the addition of polymer. Berman and Tan (1985) found that the manner in which the polymer modifies the free-jet structure is highly dependent upon the type of polymer used, the purity of the water and the initial preparation of the polymer solution. They also observed a general suppression of small-scale structures and enhancement of the mean axial velocity and the larger-scale structures in the presence of polymer additives. Little turbulent mixing was observed except very far downstream of the nozzle ($> 100D$). Koziol and Glowacki (1989) considered the influence of dilute polymer suspensions on the character of both free and impinging turbulent jets. Their free-jet results are consistent with those of Berman and Tan (1985) and their impinging-jet results indicate that the addition of polymer can significantly alter the turbulence characteristics of the impingement region and can delay the onset of turbulence in the wall-jet region where significant drag reduction was also observed. Glowacki (1989) found that polymer additives can enhance the turbulence levels in the vicinity of the stagnation point, particularly when the impinging surface is placed outside the potential core of the jet, with increases of nearly 300% observed for polymer concentrations of 50 ppm. This enhancement began to diminish for larger polymer concentrations. In addition, Glowacki (1989) observed a noted decrease in the energy content of the small scales, indicating a suppression of such structures in the presence of polymer additives. Similar suppression of turbulence in the presence of polymer additives has also been observed in opposing jets (Muller

et al., 1995). These results suggest that dilute polymer solutions may provide a means of significantly enhancing the already efficient heat-transfer characteristics of the impingement zone as well as improving the cooling, heating and cutting capabilities of turbulent jets. Unfortunately, all of the polymer literature cited herein is based upon qualitative flow visualization and single-point experimental measurements, so details regarding modifications of the complex vortex interactions that appear to dominate the impingement zone of Newtonian jets are not known. In addition, little work has been pursued to study any possible heat-transfer enhancement associated with polymer additives except for simple laminar jets (Chatterjee et al., 2002). Finally, computational studies of polymer impinging jets are scarce due to difficulties in accurately modeling the interactions between the polymer and the turbulence.

1.4 Present Effort

Given this background regarding impinging jets, particularly the high heat-transfer rates achievable in the impingement region as well as the role of turbulent structures in this phenomenon, the present effort explores the impact of dilute polymer solutions on turbulence characteristics of impinging jets. Of particular interest is the possibility that adding a minute amount of polymer to water flows might enhance the turbulence characteristics in the impingement region which may then lead to further enhancement in heat transfer at the impingement surface. Particle-image velocimetry (PIV) is used to explore this possibility for multiple polymer concentrations and the resulting flow characteristics are analyzed within the free-jet, impingement and wall-jet regions.

Chapter 2

Experimental Setup

Two-dimensional PIV measurements were made in the axial–radial ($x - r$) plane positioned along the centerline of the jet and spanning axially from the jet exit to the impingement surface and radially skewed in one direction to capture both the jet core as well as the wall jet development. These experiments were conducted with both plain water as well as two different dilute solutions of polyethylene oxide (Polyox$^{\text{TM}}$ WSR-205) in water at concentrations of 50 and 100 ppm. These two concentrations were selected based on the results of Koziol and Glowacki (1989) and Glowacki (1989), as it was observed that radial profiles of shear stress on the wall and the turbulent intensity decreased monotonically with polymer concentration until attaining a minimum at 50 ppm, followed by enhancement for increasing concentration. Based on the detailed preparation recommendations in Barker (1973) to ensure repeatability, the polymer was aged in water for approximately 24 hours, mixed gently in the master tank and then allowed to stabilize for roughly 2 additional hours prior to running an experiment. Before stabilization of the polymer solution, hollow glass spheres (Sphericel$^{\text{TM}}$ 110P8; specific weight of 1.1) of mean diameter 11 μm were added. Homogeneity in the particle distribution was achieved by allowing the particles to settle overnight in a separate tank of water whose temperature was ensured to be stable. During this time, most heavier particles settled to the bottom of the tank while the lighter particles rose to the surface. Thus, removal of these two particle populations ensured only the near neutrally-buoyant particles were employed in each experiment.

The experimental facility used in this study is shown in figure 2.1. The flow is driven by a hydraulic head in the master tank that is kept constant by means of a centrifugal pump. As pumping may induce mechanical degradation of the polymer, the experiment was designed such that the total one-pass pumping time was larger than the data acquisition time period. To reduce mixing in the master tank, an expansion was used to reduce the discharge velocity and a set of

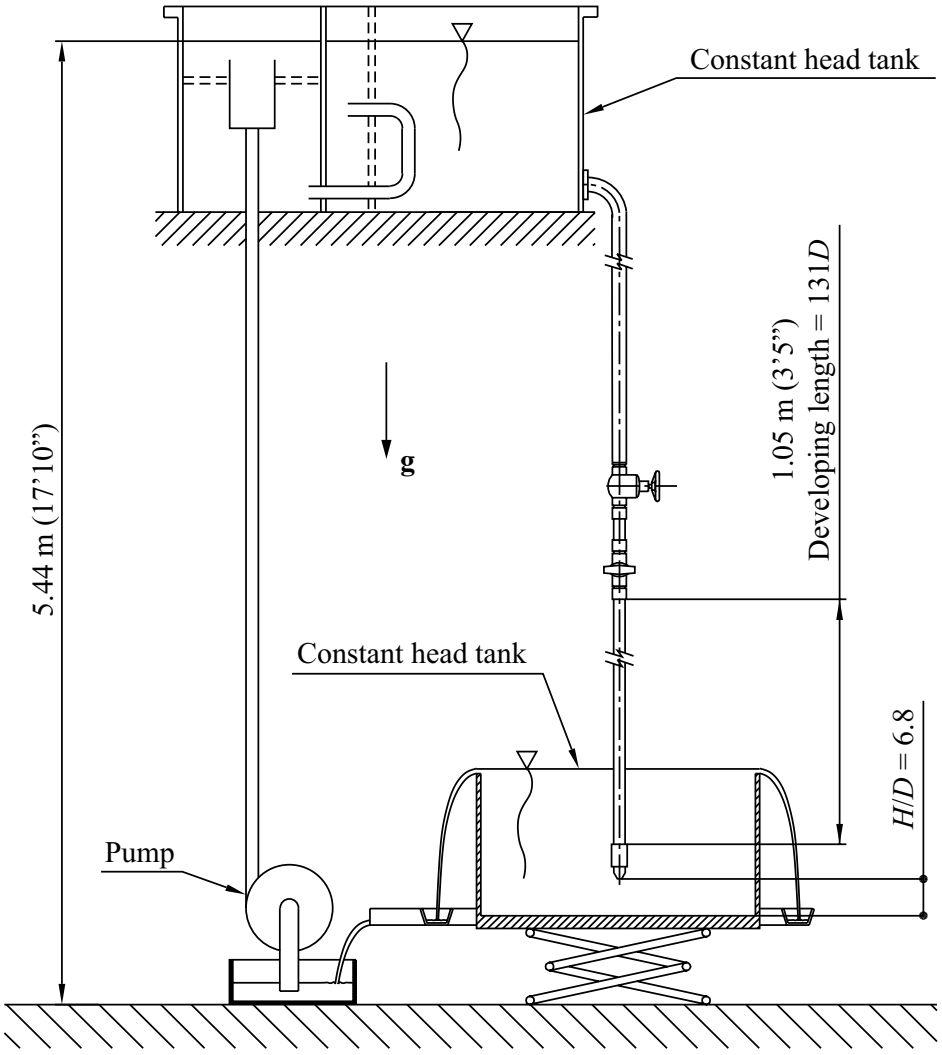

Figure 2.1: Schematic of experimental facility.

screens was employed to induce piston-like flow. With regard to nozzle geometry, recall that Barker (1973) found no effect of polymer when the flow upstream of the nozzle was laminar, even at high exit Reynolds numbers ($\mathrm{Re}_D = 50000$). Instead, he found an effect to occur when the turbulence intensity at the exit of the nozzle was high. Further, Hussain and Ramjee (1976) found the mean velocity and turbulence intensity of the core of the flow at the exit of the nozzle to be independent of its shape. However, they found the same is not true for the boundary layer at the exit of the nozzle. As a result, rapid contraction nozzles produce higher turbulence intensities and entrainment rates in the near region of jets. However, as opposed to Hussain and Ramjee (1976), Hoyt and Taylor (1979) did not find an important effect of the nozzle shape on the turbulence intensity of

the near region of the jet. They found instead that adding a straight section at the end of the nozzle enhances the levels of turbulence intensity in the near region of the jet. This is likely the most important factor since Hussain and Ramjee (1976) had a straight section at the end of the rapid contraction nozzles they employed. Given this background, the nozzle employed herein was conical in shape for simplicity in its construction. In addition, to enhance the levels of turbulence in the boundary layer at the exit, we added a straight section at the end of the nozzle. Finally, to induce higher levels of turbulence in the core of the exit flow, a fully-developed turbulent flow was ensured upstream of the nozzle. The area contraction ratio was 8:1 while the diameter and relative length of the straight section were 8 mm and $6.75D$, respectively.

With regard to the specific nozzle-to-wall distance considered herein, this choice was driven by previous observations regarding maximum stagnation-point heat transfer (see §1.2). In particular, the results of Baughn and Shimizu (1989) for $H/D = 2.0$, 6.0, 10.0, and 14.0, may be interpolated to obtain $H/D = 6.8$ as the configuration for maximum stagnation-point Nu. This was in fact the nozzle-to-wall distance used for the current experiments. Of particular interest is this arrangement is not only consistent with the occurrence of maximum heat transfer at the stagnation point, but is also consistent with the upper limit for the range of nozzle-to-wall distances showing a signature of laminar-turbulent transition as well as the upper limit for heat transfer to be enhanced in the impingement region by artificially-induced turbulence.

According to Bird et al. (1987) and Sreenivasan and White (2000), it is required to go beyond a certain onset of turbulence for the Toms effect to show up in the flow. To the best our knowledge, a metric for evaluating this onset has not been developed for free shear flows. Moreover, previous studies on impinging jets of dilute solutions of polyethylene oxide have been conducted with samples of average molecular weight 1000000 kg/Kmol (Polyox$^{\text{TM}}$ WSR-301), while the present effort employs samples of average molecular weight 600000 kg/Kmol (Polyox$^{\text{TM}}$ WSR-205) which is easier to mix and has been reported to have significant drag-reducing properties (Virk, 1975, for example). Therefore, a clear measure of the onset of the Toms effect was not available for the present experiments. As such, it was decided to operate at the highest Reynolds number possible in the facility while balancing this desire with various data acquisition limitations (acquisition rate coupled with a desire to have turbulence statistics with good statistical convergence as well as a

need to avoid utilizing polymer solution that had already passed through the pumping system and thus may have suffered some degradation). It was decided to acquire 3000 statistically independent velocity fields per fluid conditions at a rate of 1.88 s per realization. Under these conditions, each ensemble required approximately 1 hour and 34 minutes for acquisition. Considering the volume of liquid available for each experiment and the need to avoid recycling this volume due to polymer degradation concerns over the aforementioned acquisition time, the maximum jet Reynolds number possible was $\mathrm{Re}_D = 28500$. Therefore, all experiments were run at $\mathrm{Re}_D = 23000$ to ensure negligible influence of polymer degradation during each experimental run.

For the data acquisition system, a TSI PowerView 11MP camera was used in concert with a 180 mJ, double-pulsed (532 nm), Nd:YAG Quantel - *Big Sky* laser. A 0.7 mm thickness laser light-sheet was generated by means of one spherical convergent lens and one cylindrical divergent lens. The laser light-sheet was aligned with the axial–radial $(x - r)$ plane of the jet. To do this, the testing tank was emptied and a laminar jet was issued from the nozzle. The light-sheet was shot through this jet, which behaves as a transparent cylindrical rod, both magnifying light deviations and generating a secondary light-sheet due to internal reflections (see figure 2.2). The original and secondary light-sheets were made to coincide to ensure alignment. The field of view was $82.98\,\mathrm{mm} \times 54.73\,\mathrm{mm}$ in size (radial by axial) and extended axially from the exit of the nozzle to the impingement surface ($H = 6.8D$). In addition, the left edge of the field of view was located at a distance of about 10.6 mm to the left of the centerline of the nozzle. Therefore, the resultant velocity fields extended approximately $9.0D$ to the right of the stagnation point. The PIV configuration is shown in figure 2.2. All timing was controlled by a PC along with a TSI timing synchronizer. The time delay between images was $\Delta t = 65\mu s$.

For the flow currently under investigation, the magnitude and direction of fluid velocity can vary significantly depending upon the region of the flow one considers. Hence, a recursive PIV interrogation scheme was used to refine displacement detection using the TSI Insight 3G software package. In order to minimize loss of particle pairs, the second interrogation spot was larger than the first. In addition, the maximum displacement between images (which occurs in the neighborhood of the nozzle's exit) was maintained between 10 and 14 pixels. The first interrogation spot size in this interrogation scheme started at $40 \times 40\,\mathrm{pixel}^2$ and decreased in discrete steps until $32 \times 32\,\mathrm{pixel}^2$. To

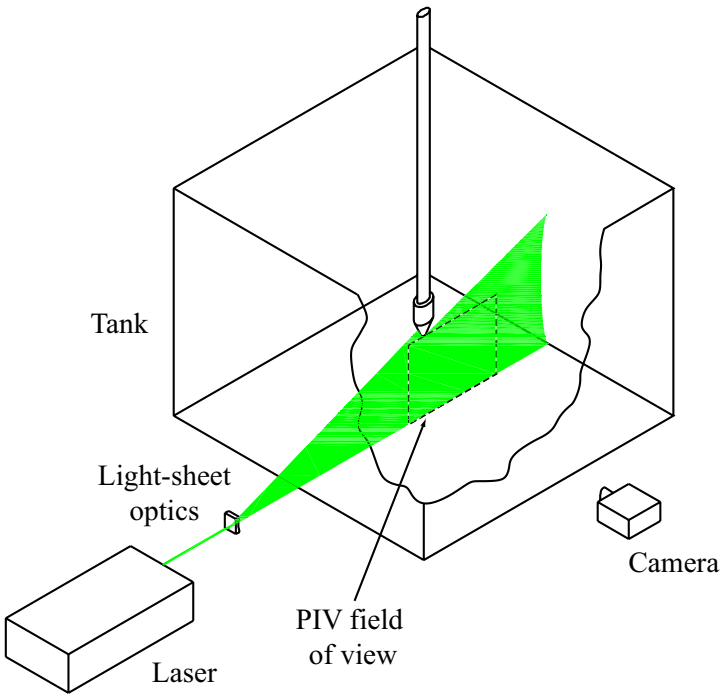

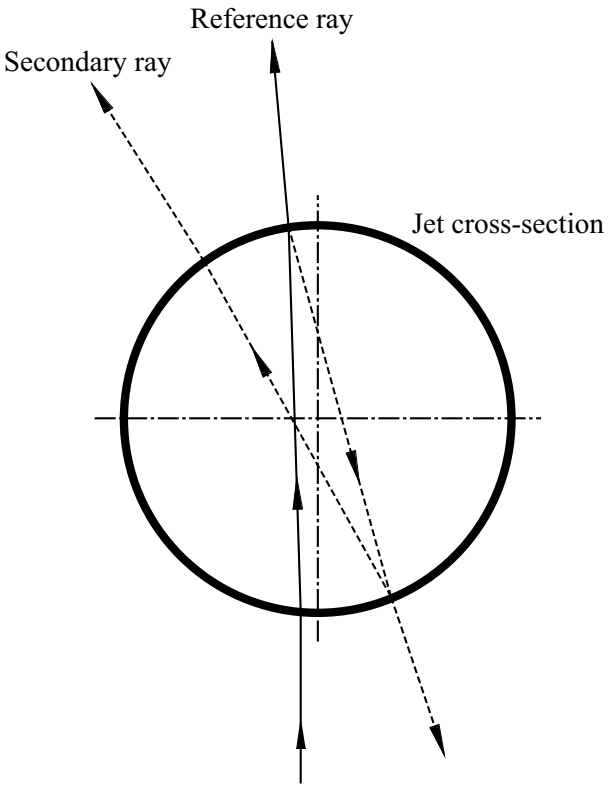

Figure 2.2: Schematic of PIV setup and laser light-sheet alignment method.

eliminate aliasing due to spatial undersampling, a 50% spot overlap was used in each interrogation step, satisfying Nyquist's criterion. The particle displacements obtained in each interrogation step were used as local offsets between the interrogation spots of the two PIV frames in the subsequent interrogation step. A pass validation was performed between successive interrogation steps to reduce the error in estimating local offsets. For each pass validation, a local median filter followed by a local mean filter were used to eliminate spurious vectors. Missing vectors were substituted with vectors estimated via neighbor interpolation followed by smoothing with a Gaussian filter. Upon completion of the iterative interrogation, the final resultant fields were validated using the above mentioned median and mean filters to eliminate spurious vectors. Following this, a Rohaly–Hart correlation [Hart (2000) and Rohaly et al. (2002), implemented by TSI Inc.] was used to replace some of the missing vectors by valid vectors. Subsequently, all remaining missing vectors were replaced by means of neighbor interpolation. Finally, a narrow Gaussian filter was used to smooth out the displacement field and reduce aliasing due to the presence of high frequency unresolved and spurious fluctuations. To minimize the number of interpolated vectors, the interrogation scheme just described was optimized to yield typically less than approximately 2% spurious vectors per field prior to final validation.

Chapter 3

Results

3.1 Instantaneous Fields

Figure 3.1a presents an instantaneous velocity field in the axial–radial ($x-r$) plane of the plain water jet. To identify embedded vortical structures in the flow, the swirling strength method is employed. Swirling strength, λ_{ci}, is the imaginary portion of the complex eigenvalues of the local velocity gradient tensor and is an unambiguous marker of rotation (Zhou et al., 1999). This methodology is frame independent and is superior to vorticity which can incorrectly mark regions of shear as having rotation. In the two-dimensional measurement planes garnered from PIV swirling strength can be calculated from an equivalent two-dimensional version of the velocity gradient tensor (Adrian et al., 2000). Further, since λ_{ci} does not embody the sense of the rotation (as the complex eigenvalues occur in complex-conjugate pairs), the sign of the local in-plane fluctuating vorticity can be used to distinguish clockwise from counter-clockwise rotating motions in the measurement plane (Wu and Christensen, 2006).

This vortex identification scheme reveals the boundaries of the jet prior to impingement to be populated by counter-rotating vortical structures, with the left portion of the jet occupied by clockwise-rotating (blue) vortices while the right portion is populated with counter-clockwise rotating (red) vortices. As the impingement surface is approached it is clear that these well-defined vortical structures of the jet interact significantly with the surface and eventually are driven along the surface in the wall-jet region. Figures 3.1b–d provide zoomed-in views to the free jet, impingement and wall-jet regions as demarcated by the boxed regions in figure 3.1a. The present PIV measurements resolve a broad range of spatial scales of the flow, from the large-scale structures characteristic of the free-jet region to the smaller scale turbulent motions that mark the impingement and wall-jet regions. Of interest, the zoomed-in views of the impingement and

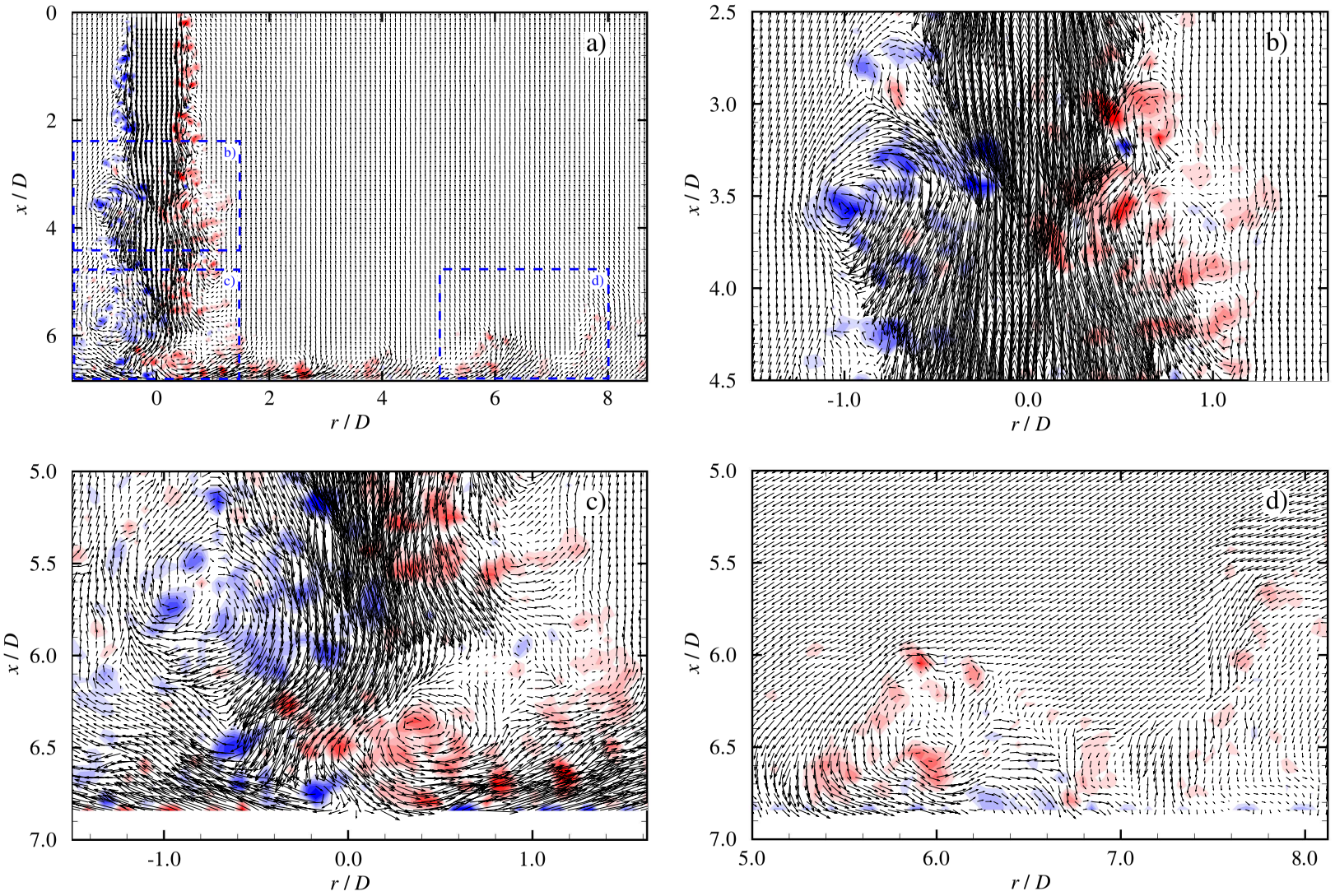

Figure 3.1: a) instantaneous PIV realization. b) zoom in the free-jet region. c) zoom in the impinging region. d) zoom in the wall-jet region.

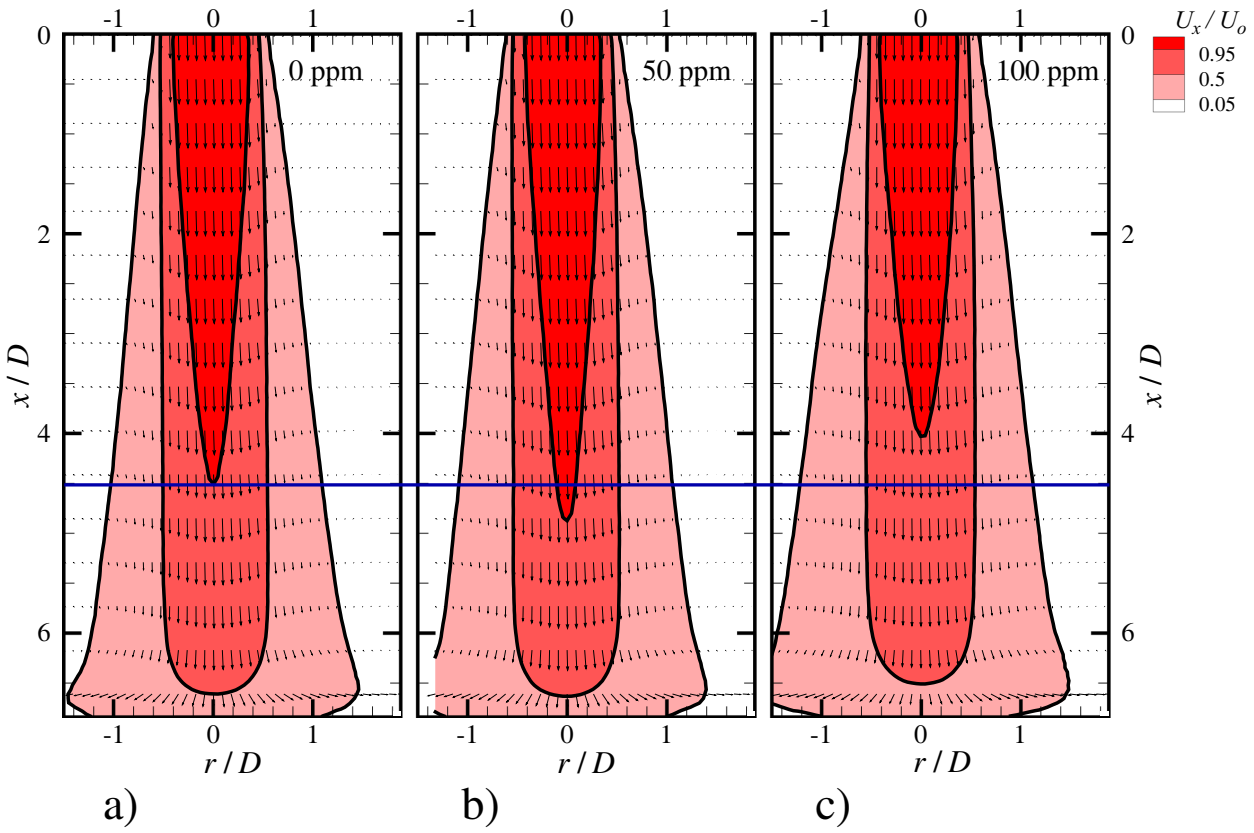

Figure 3.2: Ensemble-averaged velocity fields (vectors) for the three concentrations with contours of the axial velocity component shown in the background. Each contour demarcates one of the following features of the free jet region: potential core: $U_x/U_\circ = 0.95$; half radius contour: $U_x/U_\circ = 0.5$; jet boundary: $U_x/U_\circ = 0.05$. The horizontal blue line is used as a reference to compare the length of the potential core of the polymer solutions with respect to the one of water. Solution concentrations: a) 0 ppm, b) 50 ppm c) 100 ppm.

wall-jet regions reveal the formation of clockwise-rotating structures immediately adjacent to the surface which are commonly observed in wall-bounded turbulent flows. These structures co-exist with the counter-clockwise rotating structures that have survived the impingement process.

3.2 Average Fields

3.2.1 Free-jet region

Figure 3.2 shows the ensemble-averaged velocity fields for the three different polymer concentrations computed over the 3000 instantaneous fields per case. In addition, contours of axial (vertical)

velocity normalized by jet exit velocity, $U_x/U_\circ$, are included as well. The extent of the potential core can be visualized with the $U_x/U_\circ = 0.95$ contour and it is noted that the potential core is found to increase in length for the 50 ppm case compared to the water case while the 100 ppm case shows a shortened potential core. Of interest, the potential core for plain water (figure 3.2a) extends to $x \approx 4.5D$, which is in agreement with previous studies (Corrsin, 1943; Browand and Laufer, 1977; Vlasov et al., 1973) wherein the potential core is expected to extend to $4.0 < x/D < 5.0$, depending on the thickness of the boundary layer at the exit of the nozzle. On the other hand, for a concentration of 50 ppm (figure 3.2b), the length of the potential core is enhanced to $x/D \approx 4.8$. This observation is in agreement with the effect reported by Koziol and Glowacki (1989) and Glowacki (1989). However, for a concentration of 100 ppm, the length of the potential core is shortened to $x/D \approx 4.0$. Thus, polymer concentration, even at dilute levels, can modify the near-field development of the turbulent jet. In consequence, the width of the jet, as represented by the jet half-radius ($r_{1/2}$ = radial location where $U_x = 0.5U_\circ$), is also modified between the three cases as shown in figure 3.3a. The 50 ppm case shows the narrowest half-width while the 100 ppm case shows the largest half-width with plain water sitting in-between. These differences are in fact apparent just downstream of the jet exit but grow significantly as the impingement surface is approached.

In addition, figure 3.3b presents the centerline velocity development with axial position and it is evident that the centerline velocity departs from the jet exit velocity once the potential core is closed (Corrsin, 1943). In this regard, the change in the length of the potential core can be interpreted as a change in the spreading rate of the jet, which in turn, may be the result of one or more of the following three effects: a change in the entrainment rate of the jet, a modification of the initial thickness of the mixing layer, and/or a difference in the turbulence intensity advected by the flow before exiting the nozzle. The fact that the half-radius shows differences immediately after the jet exit may indicate a difference in the initial thickness of the mixing layer of the jets and/or to a difference in their entrainment rate.

The set of curves presented on Figure 3.4 presents normalized flow rate ($Q/Q_\circ$) driven by each free jet as it flows along its centerline. To estimate the flow rate Q of each case, the average axial velocity at fixed axial positions along each jet centerline were computed. These velocities were

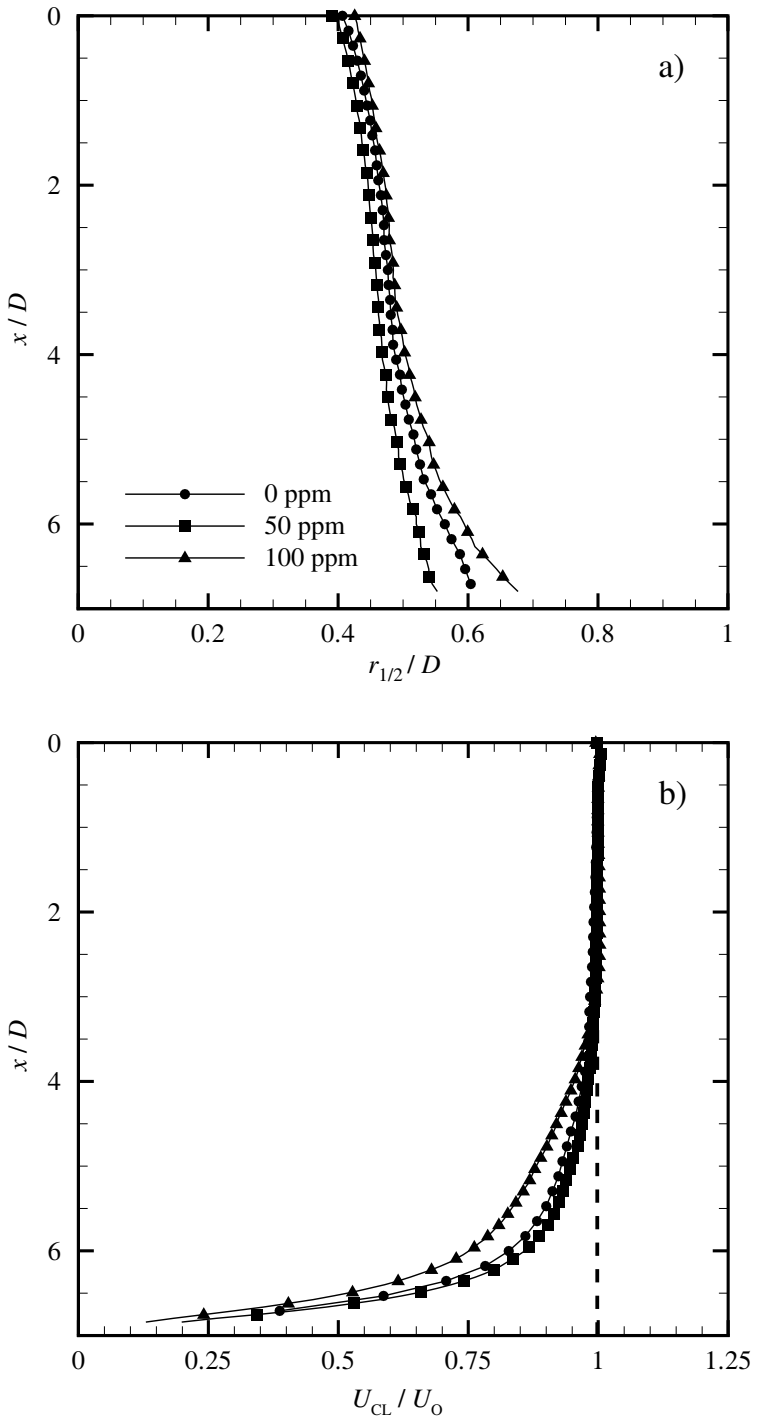

Figure 3.3: a) Jet half radius, $r_{1/2}/D$; b) Center line velocity, $U_{CL}/U_{\circ}$.

multiplied by the cross-sectional area of each jet at the corresponding axial positions along the centerline. To carry out these calculations, the outer boundary of each free jet was defined by the

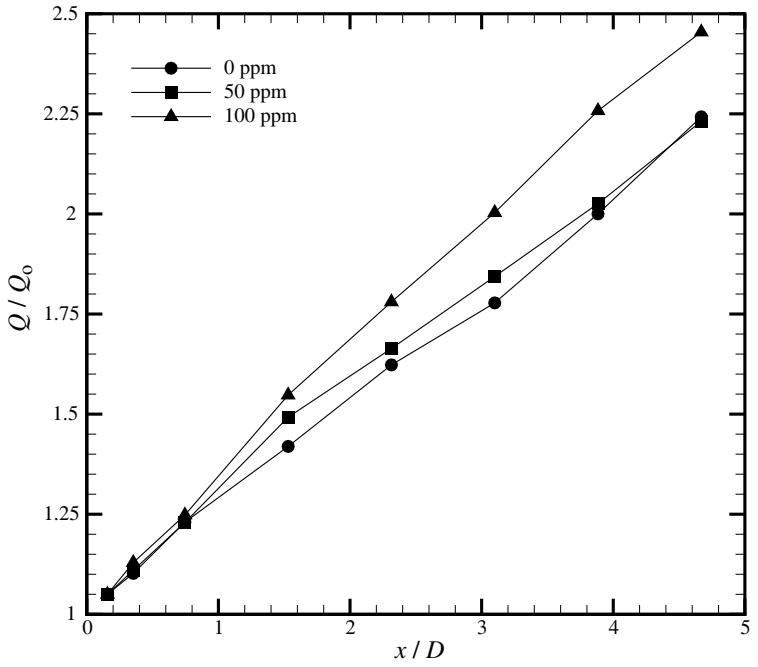

Figure 3.4: Jet flow rate normalized by flow rate at the exit of the nozzle. Flow rate increases with x/D due to entrainment.

contour $U_x/U_\circ = 0.05$ in figure 3.2. The resultant flow rates were then normalized by the flow rate at the exit of the nozzle ($Q_\circ$). Thus, the curves of normalized flow rate in figure 3.4 provide a measure of how much fluid from outside the jet core is entrained into the jet. From figure 3.4 it is evident that the near-field entrainment rate is not modified by addition of polymer as all three cases show similar behavior for $x/D < 0.75$–the straining region of the jets. Thus, the initial difference in the thickness of the jets discussed above cannot be explained by differences in entrainment rates. On the other hand, a strong enhancement in the entrainment rate of the 100 ppm jet compared to plain water is evident for $x/D > 0.75$, most notably near the impingement surface. In contrast, the enhancement in the 50 ppm jet is less pronounced and tends to collapse with the 0 ppm jet over distance.

The width of the mixing layer just downstream of the jet exit can be visualized via plots of turbulence intensity versus radial position. Figure 3.5a presents these profiles for the three concentrations and it is evident that the mixing layer very close to the nozzle's exit is thicker for the 100 ppm case compared to plain water while the 50 ppm case appears slightly thinner. In addition, the peak turbulence intensity is largest for the 100 ppm case while the 50 ppm case shows

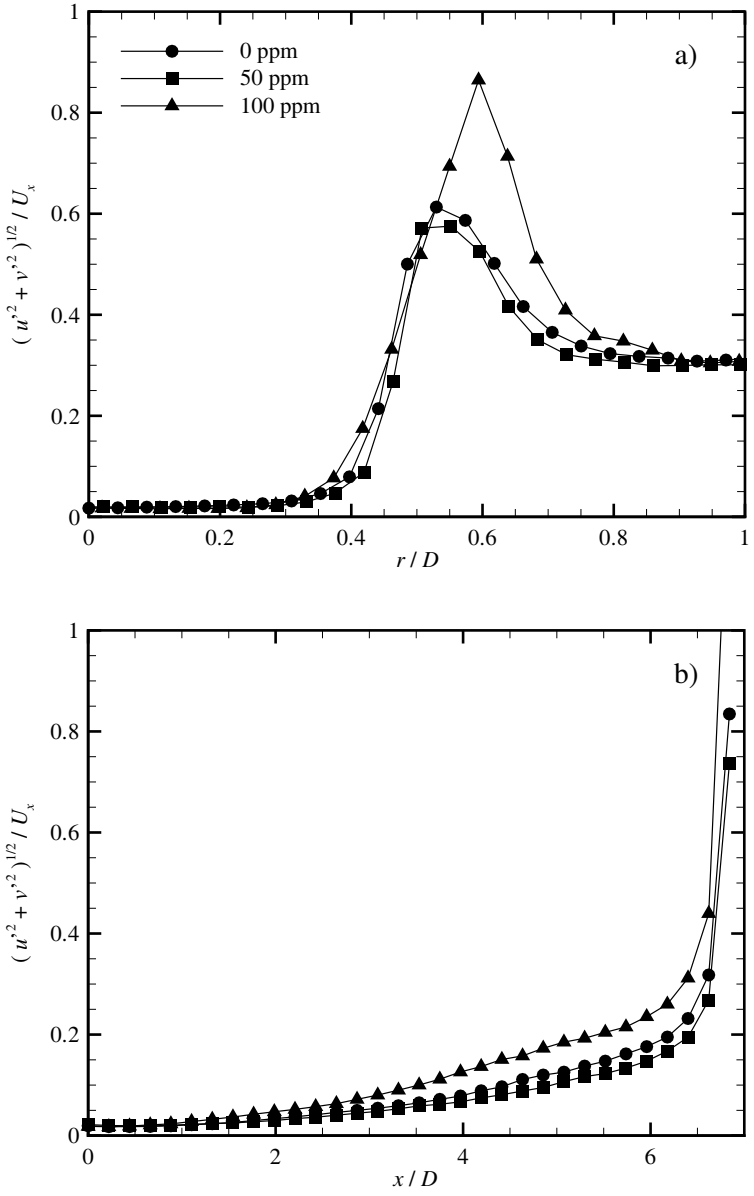

Figure 3.5: a) Radial profiles of turbulence intensity for $x/D = 0.13$. b) Turbulence intensity development along the centerline of the free jet, $(u'^2 + v'^2)^{1/2}/U_x$.

the weakest levels of turbulence. In addition, the centerline of the mixing layer of the 100 ppm jet, as inferred from the radial location of peak turbulence intensity, is farther away from the jet centerline than the plain water jet. This behavior might be due to the "die-swell" effect that can occur in viscoelastic fluids that undergo a non-zero first normal stress difference (Larson, 1998). In the case of the 50 ppm jet, such an effect is not apparent as the radial position of the peak turbulence intensity in its mixing layer matches that of plain water.

Finally, figure 3.5b presents profiles of turbulence intensity along the centerline of each jet versus axial position for the three cases. Of interest, the centerline turbulence intensity for the three cases collapse with one-another right at the exit of the nozzle. From this observation, it can be inferred that the turbulence intensity just upstream of the nozzle exit is similar in magnitude for the three cases. Thus, inlet turbulence intensity is likely not a significant factor in the lengthening/shortening of the potential core in the presence of polymer. In addition, consistent with an increase in peak turbulence intensity off of the jet centerline just downstream of the jet nozzle for the 100 ppm case (figure 3.5a), a growing enhancement in turbulence intensity is noted for this case as the impingement surface is approached. In contrast, the slight reduction in turbulence intensity noted downstream of the nozzle exit for the 50 ppm case compared to plain water persists with increasing axial position. Taken together, these effects may therefore offer satisfactory explanations for differences in jet diameters very close to the exit of the nozzle. In the case of the 50 ppm jet, reduction in the thickness of the mixing layer along with a slight reduction in peak turbulence intensity appear to be the dominant factors causing slower growth and hence a longer potential core despite a slight enhancement in the local entrainment rate in the near-nozzle region. In contrast, in the case of the 100 ppm jet, an increase in the thickness of the mixing layer as well as in peak turbulence intensity coupled with the "die-swell" effect seem to work together to enhance the radial spreading of the jet which leads to a reduced axial length of the potential core.

In conclusion, addition of POLYOX$^{\text{TM}}$ WSR-205 in submerged axisymmetric turbulent jets, induces modifications in their entrainment rates and turbulence characteristics, initial thickness of their mixing layers, and may induce viscoelastic effects such as "die-swell" at the exit of the nozzle. For dynamically similar jets (comparable Reynolds number), depending on the concentration of polymers, these combined effects may either enhance or reduce the spreading rate of the jet, shortening or elongating the potential core as a consequence. For the present case of $\mathrm{Re}_D = 23000$, the onset for enhanced spreading rate (and shortening of the potential core) of the free jet seems to occur somewhere in the range of concentrations $50\,\mathrm{ppm} < c < 100\,\mathrm{ppm}$.

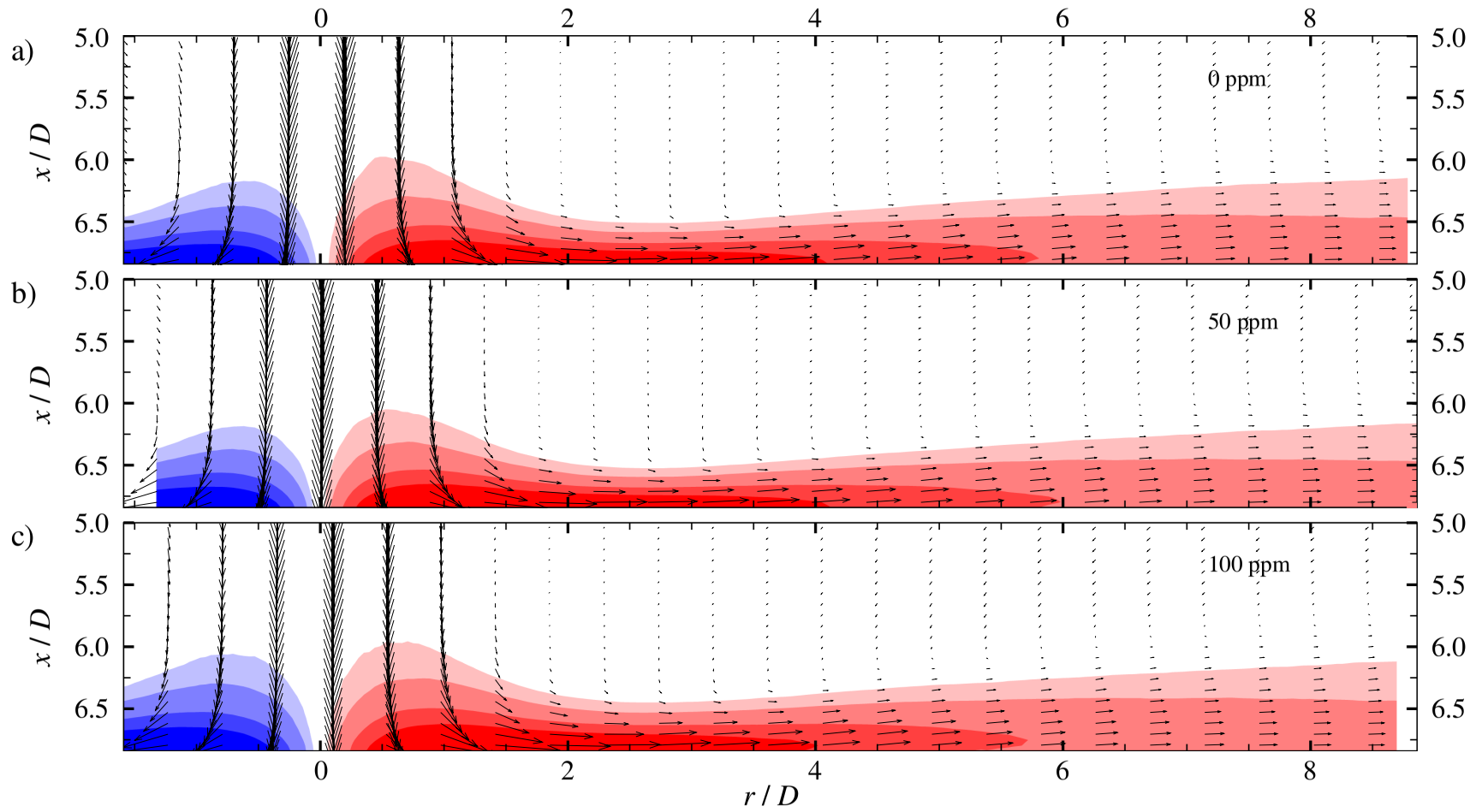

Figure 3.6: Vector field: ensemble average of velocity; Contour: radial component of the ensemble average of velocity. Jet boundary: $U_r/U_\circ = 0.05$. Solution concentrations: a) 0 ppm, b) 50 ppm c) 100 ppm.

3.2.2 Impingement and wall-jet regions

Figure 3.6 presents ensemble-averaged velocity in the impingement and wall-jet regions for the three concentrations with contours of radial velocity normalized by $U_\circ$ included in the background. For simplicity, to provide an idea of the locus of the wall jet, its boundary was defined as the region at which $U_r/U_\circ = 0.05$. The stagnation point is well defined as the boundary of the positive and negative contours at the bottom wall as is the outer boundary of the wall jet by the $U_r/U_\circ = \pm 0.05$ contour levels. Figure 3.6 is best explained in concert with figures 3.7a and 3.7b which present the half thickness of the wall jet and the peak radial velocity, respectively. The half thickness is defined as the wall-normal position at which the radial velocity of the wall jet is 50% of the peak radial velocity of the wall jet at a given radial position. On the other hand, the peak radial velocity is the highest radial velocity of the wall jet at each radial distance. It should be noted that the locus of the peak radial velocity follows a path similar to the half thickness but closer to the wall, and defines the edge of the boundary layer of the wall jet.

First, it is clear from figure 3.6 that the 100 ppm wall-jet is the thickest while the 50 ppm wall-jet is the thinnest. This could be a direct consequence of the difference in jet spreading in the free jet region. Additionally, the half thickness of the wall jet, as shown in figure 3.7, has a minimum at $r/D \approx 2.25$, which is in the neighborhood of where the velocity vectors along different streamlines become parallel to each other. In consequence, the pressure gradient present near the stagnation region may vanish at this location, which is a suitable condition for a laminar-turbulent transition to occur in the boundary layer of the wall-jet as previous studies (Cooper et al., 1993; Gardon and Cobonpue, 1962; Gardon and Akfirat, 1965) have observed this transition to occur near $r/D \approx 2.0$. We refer to the position of minimum half-width as the *neck* of the wall jet and employ this radial position as a control point to study differences in the entrainment rates along the radial coordinates for the different polymer concentrations. In this regard, figure 3.8 illustrates how the entrainment is enhanced in both polymer solutions, with the 50 ppm solution exhibiting a slightly higher enhancement than the 100 ppm solution compared to plain water.

The profiles of peak radial velocity (figure 3.7b) present a maximum in the neighborhood of $r/D \approx 1.2$. According to Koziol and Glowacki (1989) and Glowacki (1989), the radial position of this maximum is often considered the boundary between the impingement region and the wall-jet

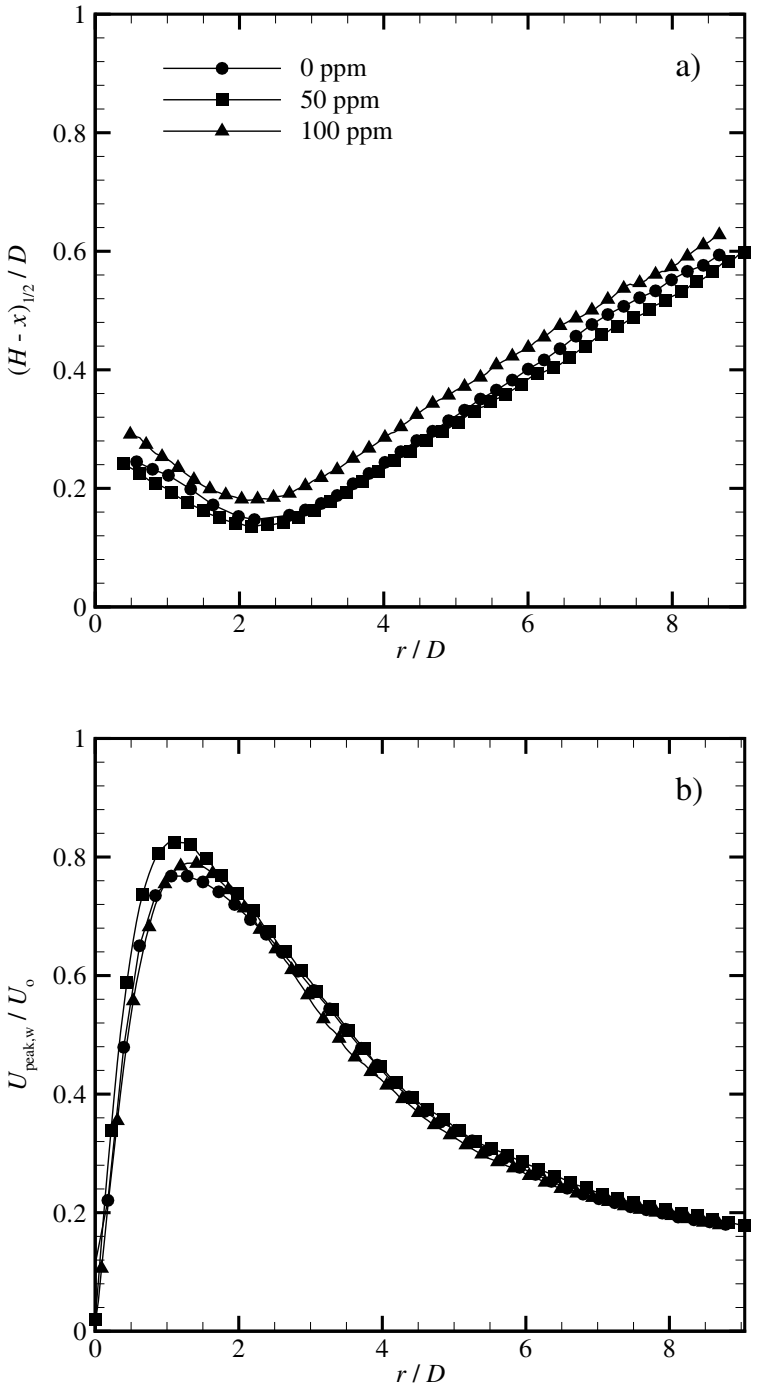

Figure 3.7: a) wall jet half height $(H - x)_{1/2}/D$; b) $U_{0wall}/U_\circ$: value of the peak velocity along the boundary layer; $(H - x)/D$: edge of the boundary layer, which is also the locus of the peak velocity in the boundary layer.

region. For the water and 50 ppm jets, the maximum occurs at $r/D \approx 1.13$, which agrees with that reported in the literature Koziol and Glowacki (1989); Glowacki (1989); Fitzgerald and Garimella

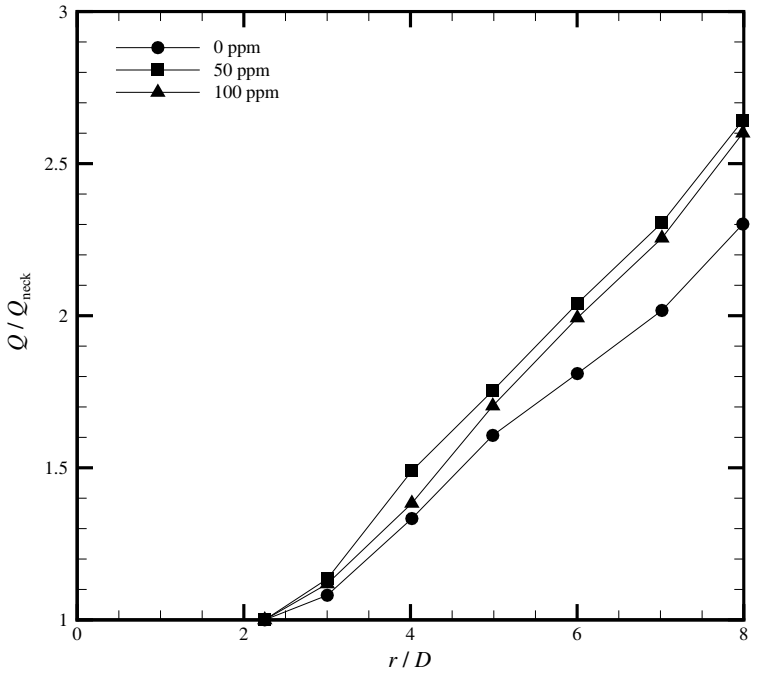

Figure 3.8: Flow rate normalized by the flow rate at the *neck* of the wall jet ($r/D \approx 2.25$). Flow rate increases with r/D due to entrainment.

(1998). However, the radial distance at which this maximum occurs for the 100 ppm jet is delayed until $r/D \approx 1.35$. Of interest, Fitzgerald and Garimella (1998) reported that the location of the maximum in peak radial velocity can move radially outward when the nozzle-to-wall distance is increased. Although the nozzle-to-wall distance is fixed in the present experiments, a shortening of the 100 ppm jet potential core was observed which can be viewed as an equivalent increase in the nozzle-to-wall distance. Beyond this observed behavior in the neighborhood of the maximum peak radial velocity, all three cases collapse further downstream in the radial direction.

3.3 Turbulence Statistics

Contour maps of turbulent kinetic energy (TKE) and Reynolds stresses, normalized with respect to the mean exit velocity, are shown in figure 3.9. These fields indicate that the 50 ppm jet contains the lowest levels of both turbulent kinetic energy and Reynolds stresses. Moreover, if attention is focused on the wall-jet region, it appears that the levels of TKE and Reynolds stresses in the 100 ppm jet are the highest and those in the 50 ppm jet are the lowest. To have a better picture

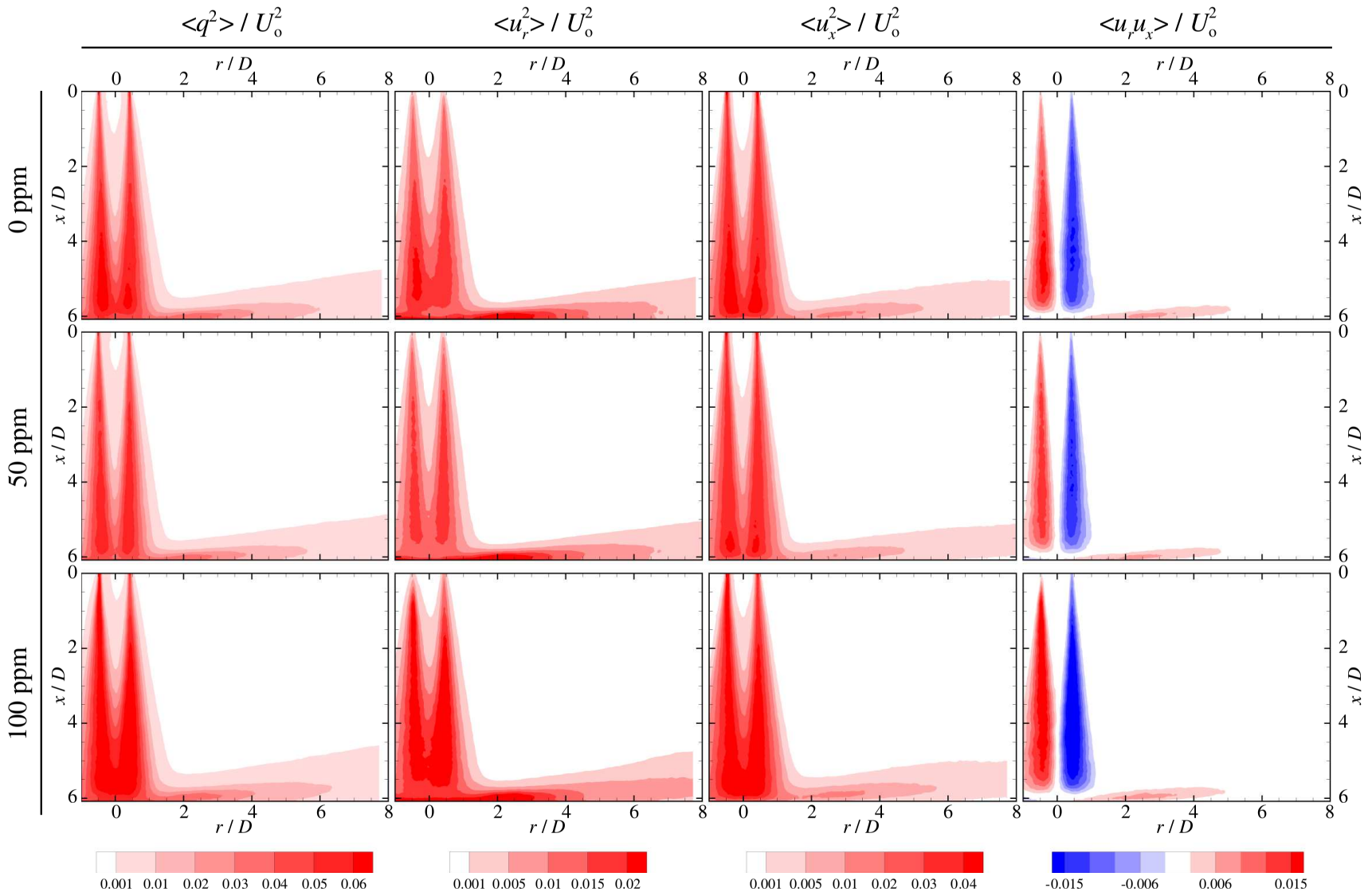

Figure 3.9: Global scalar fields. 1st column: turbulent kinetic energy, $\langle u_i' u_i' \rangle / U_\circ^2$; 2nd column: radial-normal Reynolds stress, $\langle u_r'^2 \rangle / U_\circ^2$; 3rd column: axial-normal Reynolds stress, $\langle u_x'^2 \rangle / U_\circ^2$; 4th column: shear Reynolds stress, $\langle u_r' u_x' \rangle / U_\circ^2$.

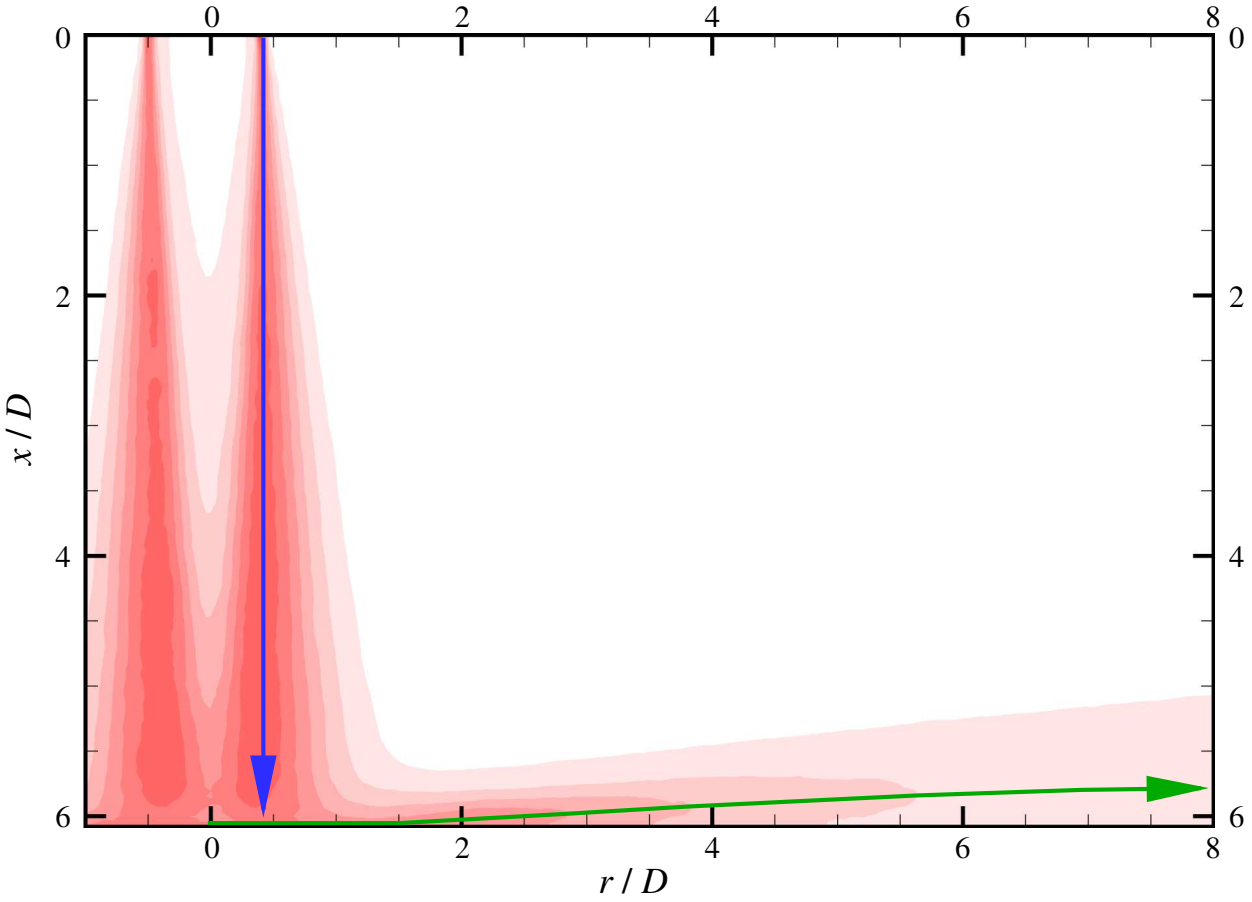

Figure 3.10: Slices taken from the two dimensional contour maps to study the variation of scalar fields in the mixing layer and in the wall jet. Blue arrow: slice along the middle line of the mixing layer; green arrow: slice along the locus of the peak of radial velocity of the wall jet.

of the dynamics of these fields, two slices were strategically taken, as illustrated in figure 3.10: one slice is along the centerline of the mixing layer in the free-jet region and the other is along the locus of peak radial velocity of the wall jet. The profiles resulting from this analysis are presented in figures 3.11–3.15.

In order to study the contribution of each of the Reynolds normal stresses in the TKE, these fields were normalized with respect to the mean exit velocity ($\langle u_i' u_i' \rangle / U_\circ^2$, $\langle u_x'^2 \rangle / U_\circ^2$, and $\langle u_r'^2 \rangle / U_\circ^2$), and are shown in figures 3.11a, b, and c. According to these figures, the TKE appears to be dominated mainly by $\langle u_x'^2 \rangle / U_\circ^2$ in the region near the nozzle exit. In the intermediate region of the free jets, $\langle u_x'^2 \rangle / U_\circ^2$ is about twice as large as $\langle u_r'^2 \rangle / U_\circ^2$. Finally, for $x/D \geq 6.5$, $\langle u_x'^2 \rangle / U_\circ^2$ decreases sharply to zero commensurate with a strong growth in $\langle u_r'^2 \rangle / U_\circ^2$. According to Cooper

et al. (1993), this increase in turbulence intensity near the wall is due to shear induced by flow acceleration near the stagnation point as the streamlines bend sharply. This is the typical behavior of a wall-bounded flow, in which the wall-normal fluctuations (coincident with axial-normal in this case) vanish and the fluctuations parallel to the wall are dominant very close to the wall. Hence, the TKE is dominated by $\langle u_r'^2 \rangle / U_\circ^2$ in the impingement region. It should be noted that there is a less obvious reduction in $\langle u_r'^2 \rangle / U_\circ^2$ that starts at $x/D \approx 5.5$ for water, $x/D \approx 4.8$ for the 50 ppm solution and $x/D \approx 4.5$ for the 100 ppm solution. This slow reduction in $\langle u_r'^2 \rangle / U_\circ^2$ appears to start in a region close to the end of the potential core (see figure 3.2), which is where the circumferential mixing layer reaches the centerline of the jet which serves as the origin of the puffing region (see figure 1.1). As a result, the reduction in $\langle u_r'^2 \rangle / U_\circ^2$ could be due to the fact that, at least in the centerline of the mixing layer, the break down of coherent structures from ring or spiral vortices to puffs affects the intensity of radial fluctuations more drastically than it affects the intensity of axial fluctuations. Note how strong this effect is in the profile of TKE of the 100 ppm solution, as it modifies the resultant profile even though the axial fluctuations do not seem to be largely affected. This effect is not as strong in the 50 ppm solution since its turbulent fluctuations are not as strong as those of the 100 ppm solution. For reference, the resultant profile of TKE for the 100 ppm case is in agreement with the results of Vlasov et al. (1973).

The TKE and Reynolds normal stresses were also normalized in a relative form with respect to the local total kinetic energy of the flow (i.e., $\langle u_i' u_i' \rangle / \langle u_i u_i \rangle$). These profiles are shown in figures 3.12a, b, and c and they can be interpreted as the percentage contributions to the total kinetic energy by the TKE and each of the normal Reynolds stresses (figures 3.12b and c). After a quantitative comparison of these profiles, one can observe that the relative TKE coincides roughly with the relative axial-normal Reynolds stress everywhere except near the nozzle exit and very close to the wall. This trend confirms that the axial velocity fluctuations dominate the TKE over most of the free-jet region. However, at the nozzle exit the radial fluctuations are large enough to affect the turbulent intensity significantly. In addition, near the wall, the decay in axial fluctuations accompanied by an increase in radial fluctuations induce a short but steep increase in the TKE. Note from figures 3.12a, b, and c how both polymer solutions display comparable behavior in the interval $0.0 < x/D < 2.2$, where they appear nearly parallel to each-other. In contrast, the

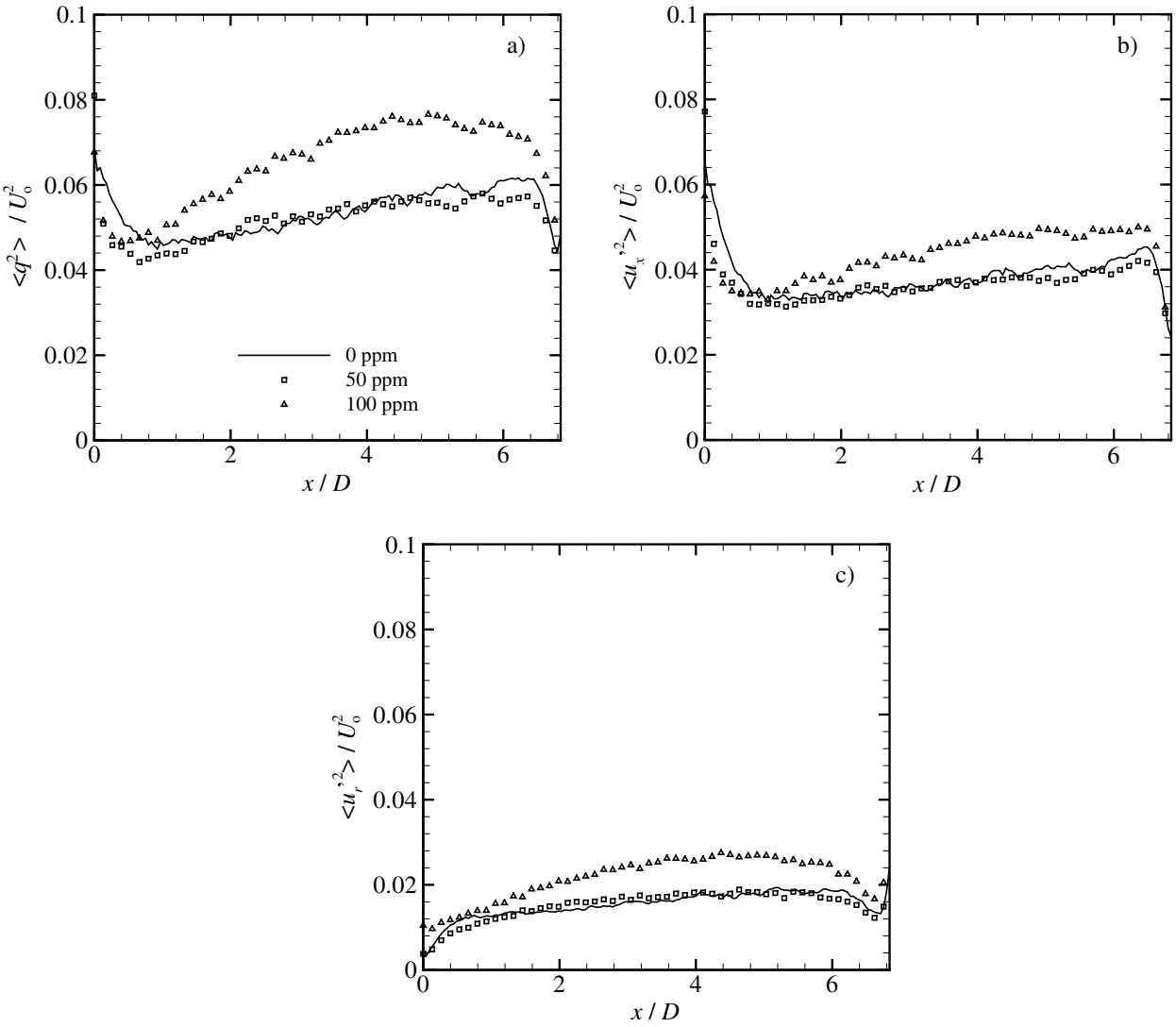

Figure 3.11: Profiles of turbulent kinetic energy and Reynolds normal stresses along the middle line of the mixing layer in the free jet region. The profiles are normalized with respect to the squared average exit velocity ($U_\circ^2$) and are called "global fields." a) Global TKE, b) global axial-normal Reynolds stress, c) global radial-normal Reynolds stress.

plain water profiles decay differently in this same interval, reaching a minimum for $x/D \approx 2.2$. Subsequently, in the interval $2.2 < x/D < 5.2$, the profiles of water and the 50 ppm solution grow at nearly the same rate. On the other hand, the profiles of the 100 ppm solution grow at a notably faster rate than the others.

Subsequently, the relative radial-normal Reynolds stress grows sharply for $x/D > 6.0$ for the water jet and the 50 ppm solution, and for $x/D > 5.7$ for the 100 ppm solution. In addition,

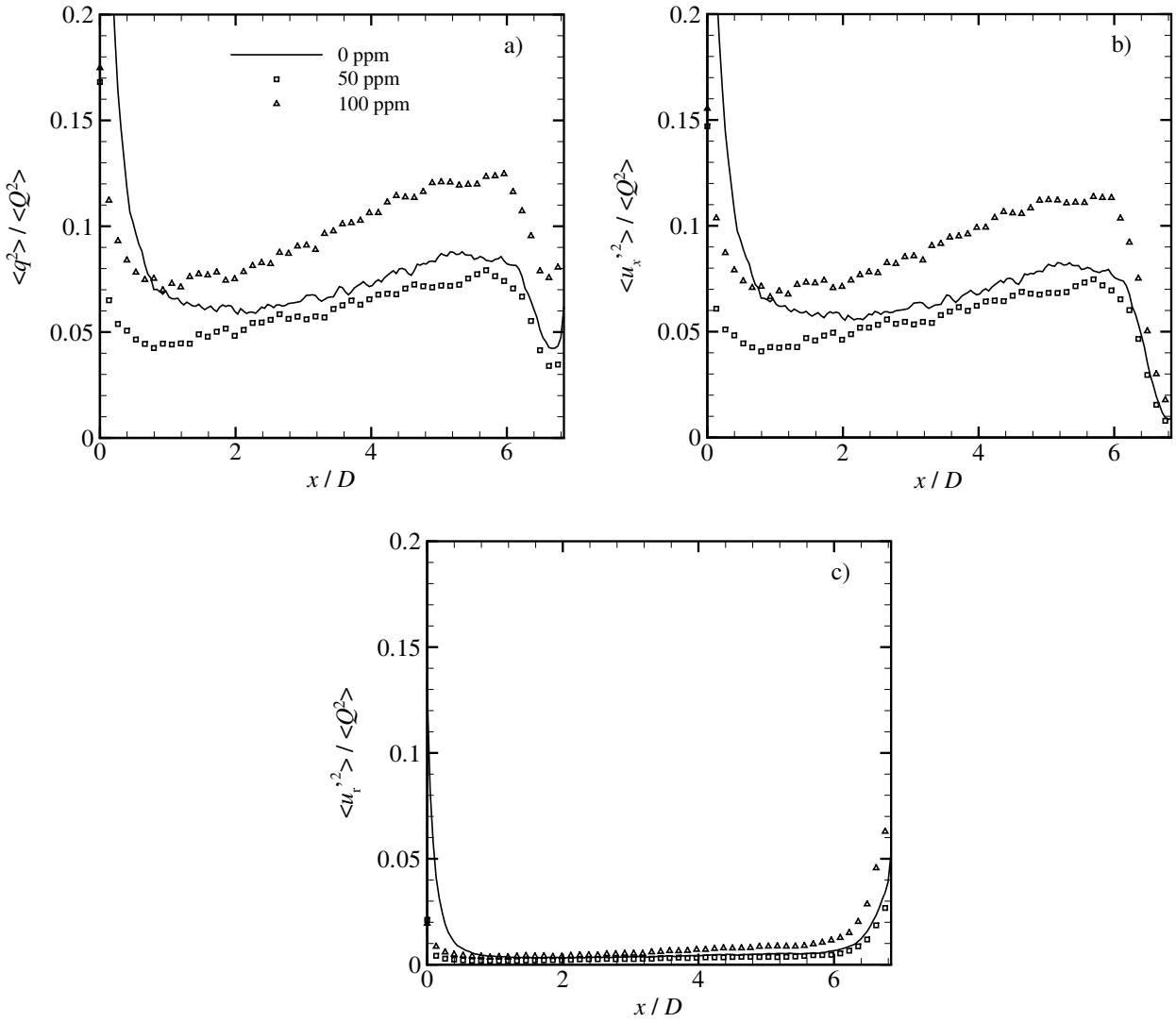

Figure 3.12: Profiles of turbulent kinetic energy and Reynolds normal stresses along the middle line of the mixing layer in the free jet region. The profiles are normalized with respect to the local total kinetic energy ($\langle u_i u_i \rangle$) and are called "relative fields." d) Relative TKE, e) relative axial-normal Reynolds stress, f) relative radial-normal Reynolds stress.

the relative axial-normal Reynolds stress drops sharply for $x/D > 6.2$ for the water jet and the 50 ppm solution, and $x/D > 6.0$ for the 100 ppm solution. The behavior of the relative normal Reynolds stresses in these intervals is consistent with the dynamics of the impingement region. That is, the TKE must be re-distributed between the turbulent fluctuations, being depleted from the axial-normal fluctuations and fed into the other components as the flow approaches the wall. Therefore, one can infer that the end of the free jet region and the start of the impingement region

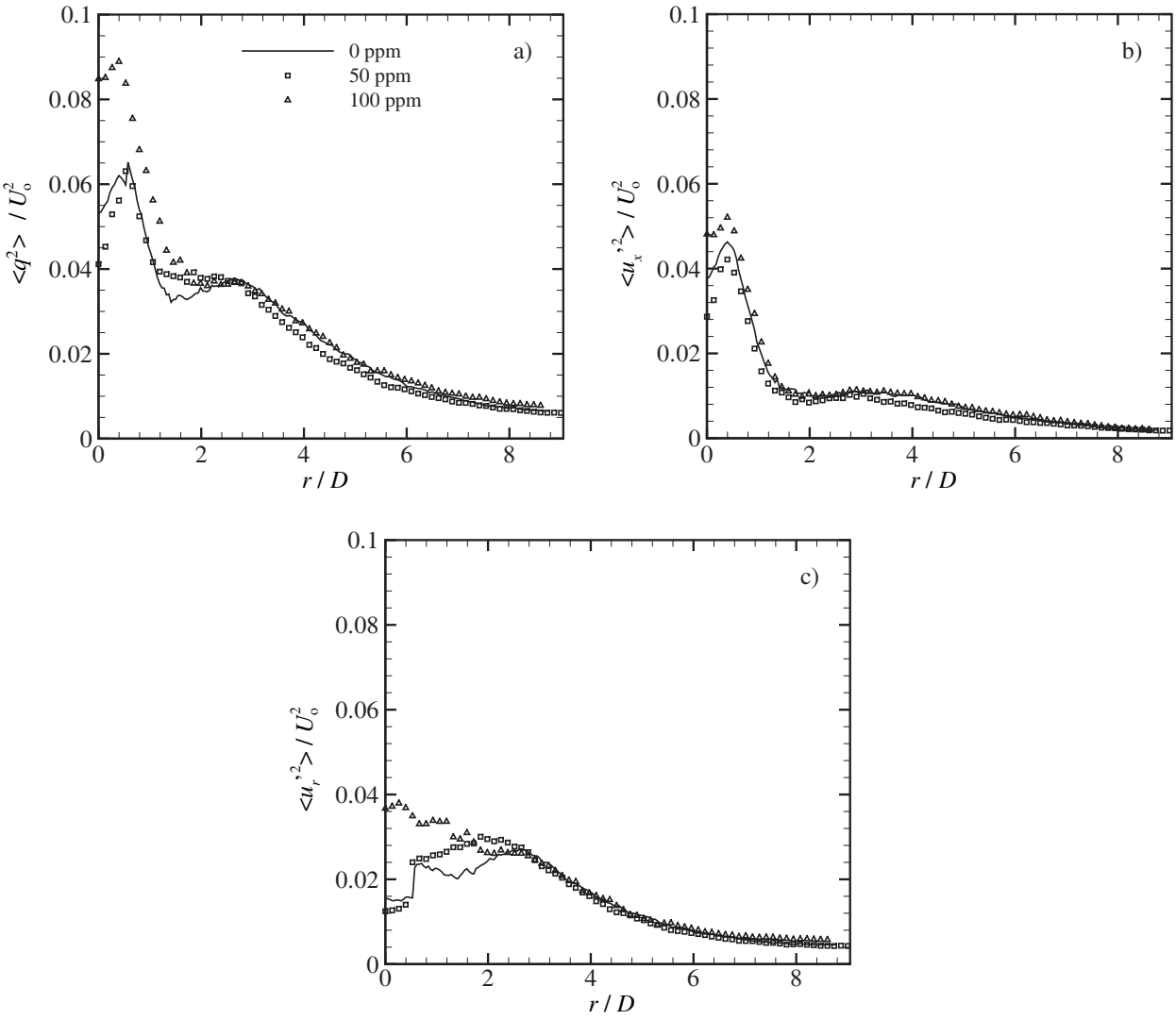

Figure 3.13: Profiles of turbulent kinetic energy and Reynolds normal stresses along the locus of the peak of radial velocity of the wall jet region. The profiles are normalized with respect to the squared average exit velocity ($U_\circ^2$) and are called "global fields." a) Global TKE, b) global axial-normal Reynolds stress, c) global radial-normal Reynolds stress.

is somewhere in the interval $6.0 < x/D < 6.2$ for the water jet and the 50 ppm solution, and in the interval $5.7 < x/D < 6.0$ for the 100 ppm solution.

As noted in the Introduction, several previous experimental efforts have shown that the Nusselt number (Nu) has local maxima at multiple locations radially away from the jet centerline, most notably for $H/D < 6$ (Gardon and Cobonpue, 1962; Popiel and Boguslawski, 1988; Baughn and Shimizu, 1989). Gardon and Akfirat (1965), referring to the observations of Corrsin (1943) in free

jets, found that the radial profile for Nusselt number coincides in shape with the radial distribution of turbulence intensity. Further, the radial location of the second local maximum in Nu is consistent with the location where secondary vortical structures are observed to form and lift from the surface (Landreth and Adrian, 1990; Sakakibara et al., 1996). Therefore, given the present configuration of $H/D = 6.8$, which is close to the range of nozzle-to-wall distances for exhibiting multiple maxima in Nu, one might expect to find non-monotonic radial distributions turbulence intensity which would imply non-monotonic behavior in convective heat transfer from the surface.

This hypothesis can be assessed in the present cases with $H/D = 6.8$ via profiles for global TKE and Reynolds normal stresses in the wall jet region as shown in figure 3.13. Based on the results of Gardon and Cobonpue (1962), for which bell-shaped radial profiles of turbulence intensity were observed in the impingement and wall-jet regions for $H/D \geq 6$, one might expect similar trends in the present cases since $H/D = 6.8$. However, as can be seen in figure 3.13, none of the present jets exhibit bell-shaped radial profiles of turbulence intensity in the impingement region. In particular, the present plain water jet case displays two clear maxima–one at $x/D \approx 0.5$ and another at $x/D \approx 2.5$–despite the present case of $H/D = 6.8$ being within the range observed by Gardon and Cobonpue (1962) to be devoid of multiple maxima. The main difference between the experiments of Gardon and Cobonpue (1962) and the present ones is that they delivered their jets from a straight pipe. Therefore, the velocity profile at the exit of their pipe corresponded to a fully developed pipe flow. As a result, the boundary layer was likely thicker at the exit of their pipe than the one at the exit of our nozzle. In consequence, the potential core in the experiments of Gardon and Cobonpue (1962) would be expected to be shorter than the present plain water jet case. Hence, the puffing region of their free jet would have ended at a shorter x/D distance than the puffing region of our free jet and hence the coherent-structure interactions at the impingement surfaces are likely quite different. Thus, a criterion based upon nozzle-to-wall distance may not provide a universal threshold with regard to the generation of multiple maxima in radial profiles of turbulence intensity. Instead, it appears that a measure based upon the length of the potential core, H/L, might provide a more accurate description of such processes.

In contrast, the present observations for the plain water jet are more consistent, at least qualitatively, with those of heat and mass transfer reported by Gardon and Cobonpue (1962), Gardon

and Akfirat (1965) and Angioletti et al. (2003) for $H/D \leq 4.0$ (see figure 3.13a). Specifically, these authors found a relative minimum at the stagnation point surrounded by an annular peak at $r/D \approx 0.5$, and a secondary peak or hump located at $r/D \approx 2.0$. Although the secondary maximum of the present plain water case occurs slightly further out near $r/D \approx 2.5$, the occurrence of multiple maxima is entirely consistent with the aforementioned studies. Interestingly, similar trends are noted in the two polymer cases, with both the 50 ppm and 100 ppm cases showing two distinct maxima. The 100 ppm is notable for a strong enhancement in the first peak in TKE compared to the plain water case while the 50 ppm case follows that of the plain water jet quite well. Consistent with previous studies, the global turbulent kinetic energy decreases monotonically with r/D thereafter, with all the curves nearly collapsing with each-other.

As discussed earlier, the potential cores of the present jets are different in length (see figure 3.2). Nevertheless, the same nozzle-to-wall distance was employed for all experiments. As a result, one should expect that the impingement wall is exposed to a different level of interaction of coherent structures and, consequently, to a different distribution of turbulence intensity for each because of these differences in the length of the potential core. In fact, it can be seen in figure 3.9 that the level of radial penetration of the mixing layer is different for each jet. In particular, it should be noted how the mixing layers of the 100 ppm jet collapse in the centerline shortly before the jet arrives at the impingement wall. On the other hand, none of the other jets' mixing layers collapse in the center line before arriving to the impingement wall. Moreover, the level of radial penetration of the mixing layers of the water and 50 ppm jets are different. Note, however, that in all cases the potential core does not reach the wall. Hence, we conclude that the impingement walls of our jets are exposed to different levels of interaction of coherent structures, but since the radial profiles of turbulent kinetic energy of all jets are non-monotonic at the wall, the walls for all jets are likely located within the puffing region. In consequence, as can be seen in figure 3.13a, the radial profile of TKE (and thus turbulence intensity) of our jets at the impingement wall are different. Nevertheless, figures 3.13b and c suggest that the radial-normal Reynolds stress is the component of the turbulent kinetic energy that is more strongly dependent on the level of radial penetration of the mixing layer, at least within the puffing region. Note that this difference affects the profiles of turbulent kinetic energy mainly in the interval $0.0 < r/D < 2.7$, modifying the magnitude of the

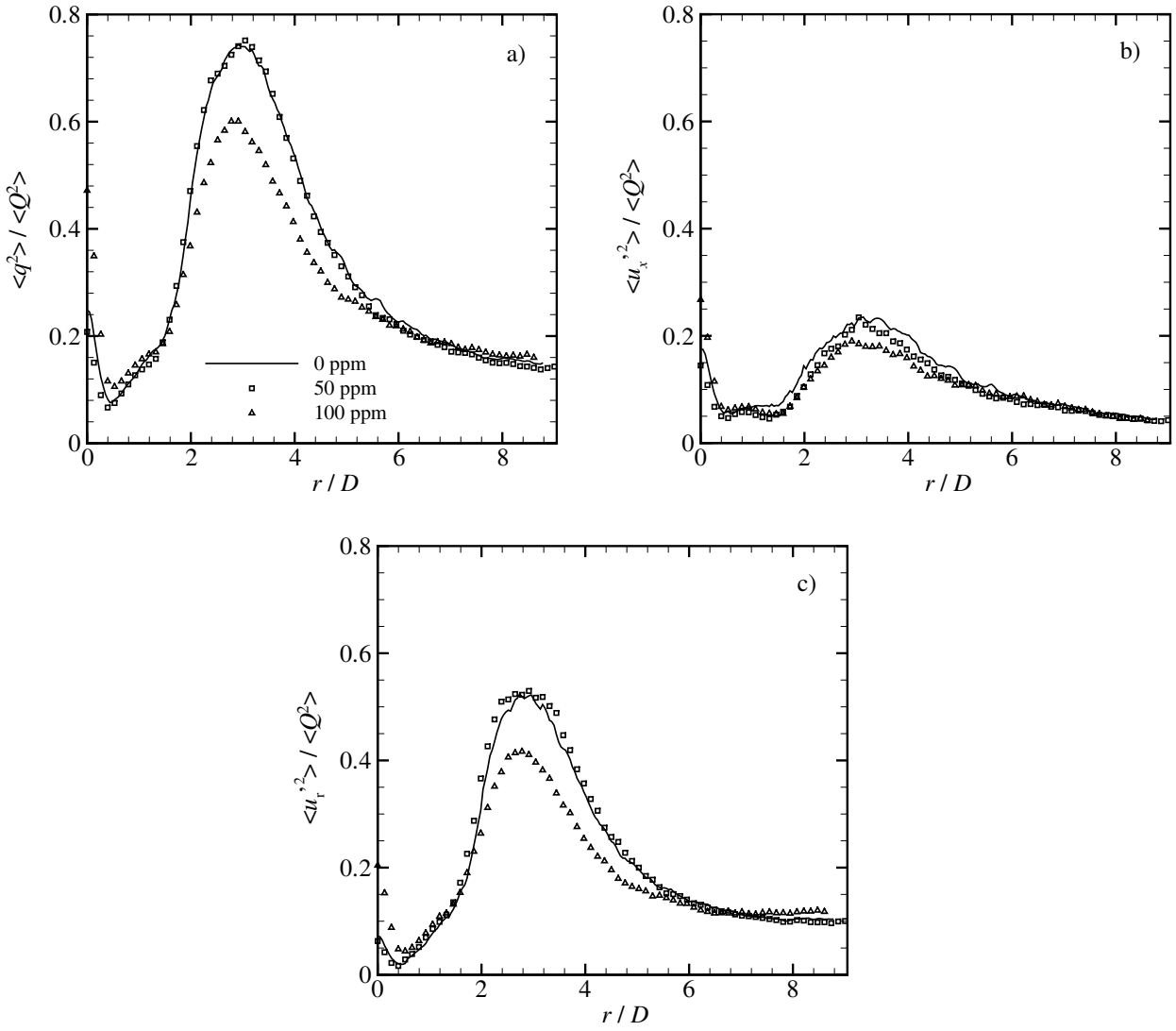

Figure 3.14: Profiles of turbulent kinetic energy and Reynolds normal stresses along the locus of the peak of radial velocity of the wall jet region. The profiles are normalized with respect to the local total kinetic energy ($\langle u_i u_i \rangle$) and are called "relative fields." a) Relative TKE, e) relative axial-normal Reynolds stress, f) relative radial-normal Reynolds stress.

primary peak and the configuration of the secondary peak.

Gardon and Cobonpue (1962) and Gardon and Akfirat (1965) pointed out that the secondary peak occurs coincident with the location at which the laminar-turbulent transition takes place in the boundary layer. Roughly speaking, the authors seem to have identified an important feature of impinging jets. However, a more detailed picture of this transition may be obtained if the TKE and Reynolds normal stresses are normalized with respect to the local total kinetic energy, as shown

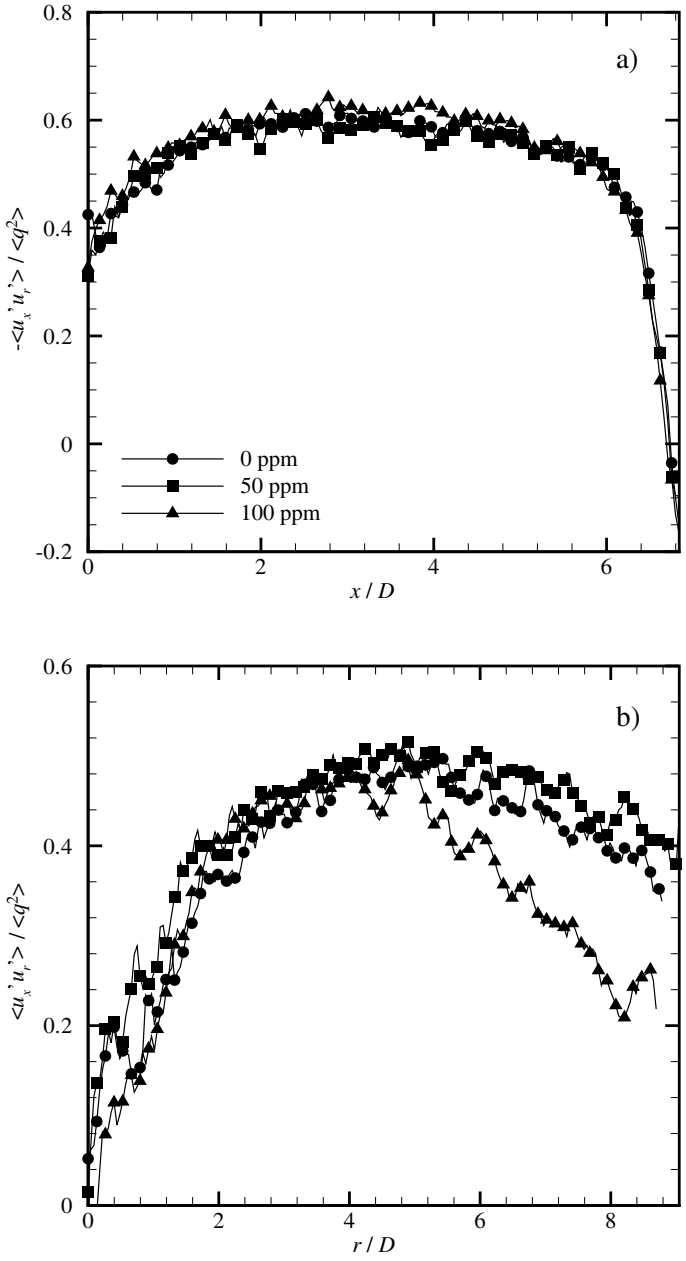

Figure 3.15: Reynolds shear stress. These curves are normalized with respect to the local TKE ($\angle u_i' u_i'\rangle$). a) Reynolds shear stress along the middle line of the mixing layer in the free jet region, b) Reynolds shear stress along the edge of the boundary layer in the wall jet region.

in figures 3.14a, b, and c. These figures have several features that help clarify and support some of the analysis already carried out about the wall jet region. First, according to figures 3.14a, b, and c, the boundary between the impingement region and the wall jet region seems to be located at $r/D \approx 0.5$, the point at which the single-point statistics reach their respective minima.

Subsequently, in the interval $0.5 < r/D < 1.5$, the axial-normal Reynolds stress remains constant while the radial-normal Reynolds stress grows steadily at a relatively slow rate, consistent with the growth of a laminar boundary layer. Subsequently, at $r/D \approx 1.5$ the TKE as well as both Reynolds normal stresses begin to grow sharply, and continue to do so in the interval $1.5 < r/D < 3.0$. This behavior is consistent with a boundary layer transitioning to turbulence, since the secondary peak of the globally normalized profiles (figures 3.13a, b, and c) that Gardon and Cobonpue (1962) and Gardon and Akfirat (1965) recognized as the location at which the laminar-turbulent transition takes place, lie within this interval. Additionally, as was mentioned in §3.2, the velocity vectors along different stream lines in the neighborhood of $r/D \approx 2.25$ tend to be parallel to each other, which is a signature of vanishing pressure gradients and hence a favorable condition for a laminar-to-turbulent transition (Cooper et al., 1993). All profiles peak in the neighborhood of $r/D \approx 3.0$, right after which the TKE and Reynolds normal stresses decay sharply in the interval $3.0 < r/D < 5.4$. Following this first decay, all profiles collapse with each other and decay monotonically as the wall jet spreads out radially. Note that, while the radial profiles of the 50 ppm solution and water collapse with each other along the wall jet, the profiles for the 100 ppm solution are reduced within the interval $1.5 < r/D < 5.4$. This behavior is consistent with polymer-induced turbulence suppression as is well-known in wall-bounded flows.

As can be seen in figure 3.15a, the Reynolds shear stresses along the middle line of the shear layer of the free jet region of all solutions collapse with each other. This indicates that the relative dynamics of the Reynolds shear stress is the same for all jets in the free jet region. The situation in the wall jet region, however, is different. When normalizing the Reynolds shear stress with respect to the local TKE, two main regions can be identified. In the first of them, located in the interval $0.0 < r/D < 5.0$, the Reynolds shear stress for all concentrations grows monotonically with r/D. Its value reaches a maximum at the end of that interval and decays monotonically thereafter in the second region ($r/D > 5.0$). The curves for water and the 50 ppm solution collapse for $r/D > 5.0$, but the one for the 100 ppm solution decays faster than the others. This difference in decaying rate may be the manifestation of the Toms effect for the 100 ppm solution. Note that the radial location $r/D \approx 5.0$ coincides with the end of a sharp decay in the TKE and radial-normal Reynolds stress (see figures 3.14a and c).

3.4 Proper Orthogonal Decomposition (POD) Analysis

3.4.1 Background

A fluid flow field, $\mathbf{u}(\mathbf{x}, t)$, is expected to contain finite kinetic energy and will obey conservation of momentum and mass. A direct consequence of the first condition is that such fields may be considered to belong to the Hilbert space of square integrable functions $L^2[\Omega]$ (Doering, 2009), where Ω defines the spatio-temporal domain $\Omega = [X, T]$. It follows that it is possible to find a decomposition for $\mathbf{u}(\mathbf{x}, t)$ in terms of a unique set of orthonormal basis $B \in L^2[X, T]$ (Dunford and Schwartz, 1988). Note that $\mathbf{u}(\mathbf{x}, t)$ as a fluid flow field is simply a subspace of $L^2[X, T]$. Obviously, any property we find for all the members of $L^2[X, T]$, will be automatically inherited by any fluid flow field $\mathbf{u}(\mathbf{x}, t) \in L^2[X, T]$. Therefore, we may consider $\mathbf{u}(\mathbf{x}, t)$ more generally as any complex valued function contained in $L^2[X, T]$. Henceforth, following Aubry (1991), this analysis makes no assumption of ergodicity or statistical stationarity for $\mathbf{u}(\mathbf{x}, t)$. Moreover, the spatio-temporal domain $[X, T]$ is allowed to be either continuous or discrete. This fact has the direct implication that $\mathbf{u}(\mathbf{x}, t)$ may be taken as a signal collected at a finite number of spatial (X) and temporal (T) points, which is the case of experimental and numerical data. Furthermore, the condition of orthonormality implies a decomposition in terms of two independent sets of basis functions: $\phi(x) \in X$ and $\psi(t) \in T$, both contained in $L^2[X, T]$. It is in this regard that this decomposition is referred to as the *Biorthogonal decomposition*.

In what follows, the biorthogonal decomposition of the signal $\mathbf{u}(\mathbf{x}, t)$ will be derived [for a more detailed derivation, see Aubry et al. (1991)]. Since any Hilbert space is an inner product space that is also a complete metric with respect to the inner product, we may use the signal $\mathbf{u}(\mathbf{x}, t)$ to construct a linear operator $U : L^2[\Omega] \rightarrow L^2[\Omega]$ as

$$(U\cdot)(\Omega) = \int_{\Omega} \mathbf{u}(\mathbf{x}, t)(\cdot)\mathrm{d}\Omega, \tag{3.1}$$

where U is a compact operator in the Hilbert space of square integrable functions $L^2[\Omega]$ (Aubry et al., 1991). In general, compact operators in Hilbert spaces have only discrete spectra which may be diagonalized by the orthonormal basis of the operator. It follows that the spectral decomposition

of U is of the form

$$(U\cdot)(t) = \sum_{k=1}^{\infty} \alpha_k \left(\cdot, \phi_k(\mathbf{x})\right) \psi_k(t). \tag{3.2}$$

Without loss of generality, if the spectral form of U is applied to an arbitrary spatial function $\phi \in L^2[X]$, and we compare the result with eq. (3.1) applied to the same arbitrary spatial function $\phi \in L^2[X]$, we find that the signal $\mathbf{u}(\mathbf{x}, t)$ has a singular value decomposition (SVD) of the form

$$\mathbf{u}(\mathbf{x}, t) = \sum_{k=1}^{\infty} \alpha_k \overline{\phi_k(\mathbf{x})} \psi_k(t). \tag{3.3}$$

From this formulation, we may develop a new operator $L^2[\Omega] \to L^2[\Omega]$ that is compact with respect to its original subspace (that is, $L^2[X] \to L^2[X]$ or $L^2[T] \to L^2[T]$). If we apply U to its adjoint U^* and vice versa, we obtain the operators U^*U and UU^* as

$$\alpha_k^2 \phi_k = \int_X r(\mathbf{x}, \mathbf{x}') \phi_k(\mathbf{x}') \, \mathrm{d}\mathbf{x}' \quad \text{where,} \quad r(\mathbf{x}, \mathbf{x}') = \int_T \mathbf{u}(\mathbf{x}', t) \overline{\mathbf{u}(\mathbf{x}, t)} \mathrm{d}t, \tag{3.4}$$

and

$$\alpha_k^2 \psi_k = \int_T l(t, t') \psi_k(t') \, \mathrm{d}t' \quad \text{where,} \quad l(t, t') = \int_X \mathbf{u}(\mathbf{x}, t') \overline{\mathbf{u}(\mathbf{x}, t)} \mathrm{d}\mathbf{x}. \tag{3.5}$$

In this context, $r(\mathbf{x}, \mathbf{x}')$ and $l(t, t')$ are the spatial and temporal correlation functions of the signal $\mathbf{u}(\mathbf{x}, t)$ respectively. Equations (3.4) and (3.5) are Fredholm integral equations of the second type. It follows from the Hilbert–Schmidt theorem that the eigenfunctions ϕ_k and ψ_k of these eigenvalue problems are orthogonal, their eigenvalues α_k^2 are positive and the signal $\mathbf{u}(\mathbf{x}, t)$ can be fully reconstructed in terms of these eigenfunctions. In this context, the eigenfunction of a given provide a measure of the relative energy content of the original signal contained in that mode. This is the essence of the Proper Orthogonal Decomposition (POD) methodology (Holmes et al., 1996; Cazemier et al., 1998). In the special case of a signal with no time coherence, like in the present work, or that has been acquired at time intervals longer than the characteristic correlation timescale of the signal, eq. (3.5) loses its meaning. In consequence, only the spatial eigenfunctions found in the eigenproblem of eq. (3.4) would be used for reconstructing the original signal. This special case is typically known as *snapshot POD* (Sirovich, 1987). The above analysis clearly shows that POD is simply a subdivision of SVD. Epps and Techet (2009) illustrated the same consistency

between SVD and POD using matrix algebra.

It should be noted that experimental data is never continuous. Instead, it should be thought of as a collection of variables measured with a set of probes located discretely at a finite number of spatial locations with sampling occurring at a finite number of times. To analyze experimental data arranged in such a form, it is convenient to express the SVD in matrix form. From eq. (3.3), the SVD of a set of experimental data contained in matrix $\mathbf{U}$ may be expressed as (Chatterjee, 2000; Epps and Techet, 2009))

$$\mathbf{U} = \mathbf{\Psi}\mathbf{\Lambda}\mathbf{\Phi}^{\mathrm{T}}, \tag{3.6}$$

where $\mathbf{\Psi}$ is a square matrix of size $[T \times T]$, whose columns are the temporal eigenvectors of $\mathbf{U}$ (representing the temporal eigenfunctions ψ_k), $\mathbf{\Lambda}$ is a rectangular diagonal matrix of size $[T \times D]$, whose diagonal elements are the singular values of $\mathbf{U}$ (representing α_k) and $\mathbf{\Phi}$ is a square matrix of size $[D \times D]$, whose columns are the spatial eigenvectors of $\mathbf{U}$ (representing the spatial eigenfunctions ϕ_k). Note that matrices $\mathbf{\Psi}$ and $\mathbf{\Phi}$ are normalized such that the Euclidian norm of their columns is unity. Therefore, the temporal and spatial shapes of the modes are given by the columns of $\mathbf{\Psi}$ and $\mathbf{\Phi}$ while the magnitude of the modes is given by their respective singular values embodied in $\mathbf{\Lambda}$. Note further that a given mode k would be expressed as the matrix $\mathbf{U}_k$ as

$$\mathbf{U}_k = \mathbf{\Psi}(1:T,k) \cdot \mathbf{\Lambda}(k,k) \cdot \mathbf{\Phi}(k,1:D)^{\mathrm{T}}. \tag{3.7}$$

To retrieve a low-order reconstruction of signal $\mathbf{u}(\mathbf{x},t)$, we simply truncate the series in eq. (3.3) at $k = M$ as

$$\mathbf{u}(\mathbf{x},t)_{low} = \sum_{k=1}^{M} \alpha_k \overline{\phi_k(\mathbf{x})} \psi_k(t), \tag{3.8}$$

where $M \ll T$ is finite and expresses the number of modes kept in the reconstruction. Since the modes are arranged in decreasing energy content and the lowest orders typically embody the largest scales of the signal, this low-order reconstruction can also be thought of as a reconstruction of the larger scales of the signal. On the other hand, the modes excluded from the low-order reconstruction, that generally embody smaller scales of the signal, yield a commensurate residual

signal of the form

$$\mathbf{u}(\mathbf{x},t)_{residual} = \mathbf{u}(\mathbf{x},t) - \mathbf{u}(\mathbf{x},t)_{low} = \sum_{k=M+1}^{\infty} \alpha_k \overline{\phi_k(\mathbf{x})} \psi_k(t). \tag{3.9}$$

When the signal is decomposed using the matrix form of SVD, as is the case of discrete signals, a low-order model would be obtained by maintaining non-zero only those diagonal elements of matrix Λ corresponding to the modes to be included in the reconstruction. Thus, all remaining diagonal elements are assigned the value of zero and the matrix of singular values would be given by

$$\mathbf{\Lambda}_{low} = \begin{cases} \mathbf{\Lambda}_{kk} = \alpha_k \ , & k \leqslant M \\ \mathbf{\Lambda}_{kk} = 0 \ , & k > M \\ \mathbf{\Lambda}_{ij} = 0 \ , & i \neq j \end{cases} \tag{3.10}$$

while the low-order SVD would be written as

$$\mathbf{U}_{low} = \mathbf{\Psi}\mathbf{\Lambda}_{low}\mathbf{\Phi}^{\mathrm{T}}. \tag{3.11}$$

Likewise, the residual reconstruction of $\mathbf{U}$ would be based on the matrix of eigenvalues given by

$$\mathbf{\Lambda}_{residual} = \mathbf{\Lambda} - \mathbf{\Lambda}_{low} = \begin{cases} \mathbf{\Lambda}_{kk} = 0 \ , & k \leqslant M \\ \mathbf{\Lambda}_{kk} = \alpha_k \ , & k > M \\ \mathbf{\Lambda}_{ij} = 0 \ , & i \neq j \end{cases} \tag{3.12}$$

while the residual reconstruction is expressed in matrix form as

$$\mathbf{U}_{residual} = \mathbf{\Psi}\mathbf{\Lambda}_{residual}\mathbf{\Phi}^{\mathrm{T}}. \tag{3.13}$$

As was mentioned earlier, the set of two-dimensional velocity fields composing the present work lack of time coherence. In other words, our PIV realizations are statistically-independent. In consequence, the method we will use to study the spatial coherence of our results is the snapshot POD. Basically, we will compute the SVD of our ensemble as given by eq. (3.6), and drop matrix $\mathbf{\Psi}$ to recover strictly spatial SVD modes. This is the methodology employed to perform POD

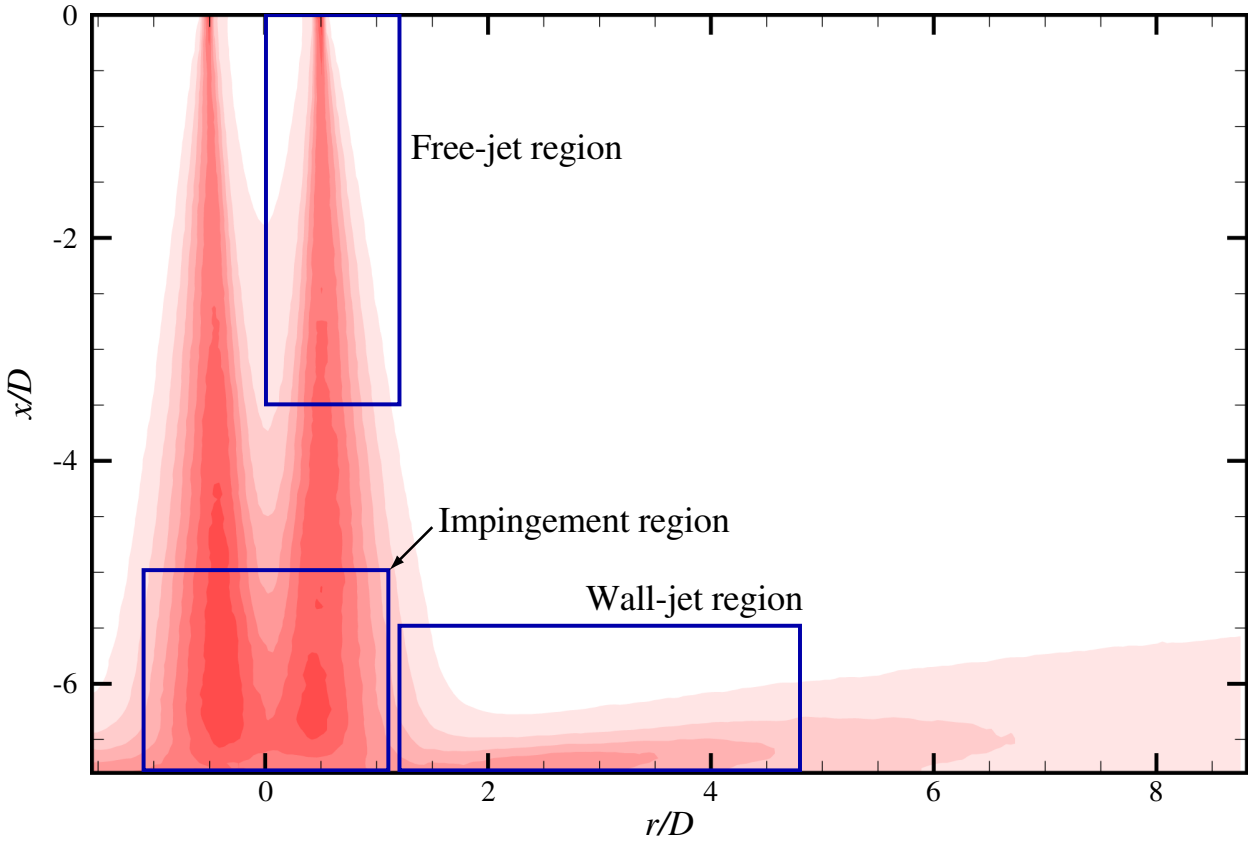

Figure 3.16: Schematic illustrating the three regions of the flow (free-jet, impingement and wall-jet regions) wherein POD analysis is performed.

analysis on the free-jet, impingement and wall-jet regions of the flow for the plain water, 50 ppm and 100 ppm cases. Figure 3.16 presents a schematic illustrating the spatial domains of the three distinct flow regions under consideration. First the energy spectra within each region is compared to assess whether the addition of polymer promotes a redistribution of the TKE as a function of scale. The first few spatial basis functions are then contrasted between the three cases within these regions of the flow.

3.4.2 Free-jet region

Figure 3.17 presents the energy spectra and cumulative energy distribution in the free-jet region demarcated in figure 3.16 for the 0 ppm, 50 ppm and 100 ppm cases. Recalling that the lowest-order POD modes embody the largest spatial scales, the energy spectra in the free-jet region reveal a clear reduction in the TKE content of the largest scales in the 50 ppm case compared to the

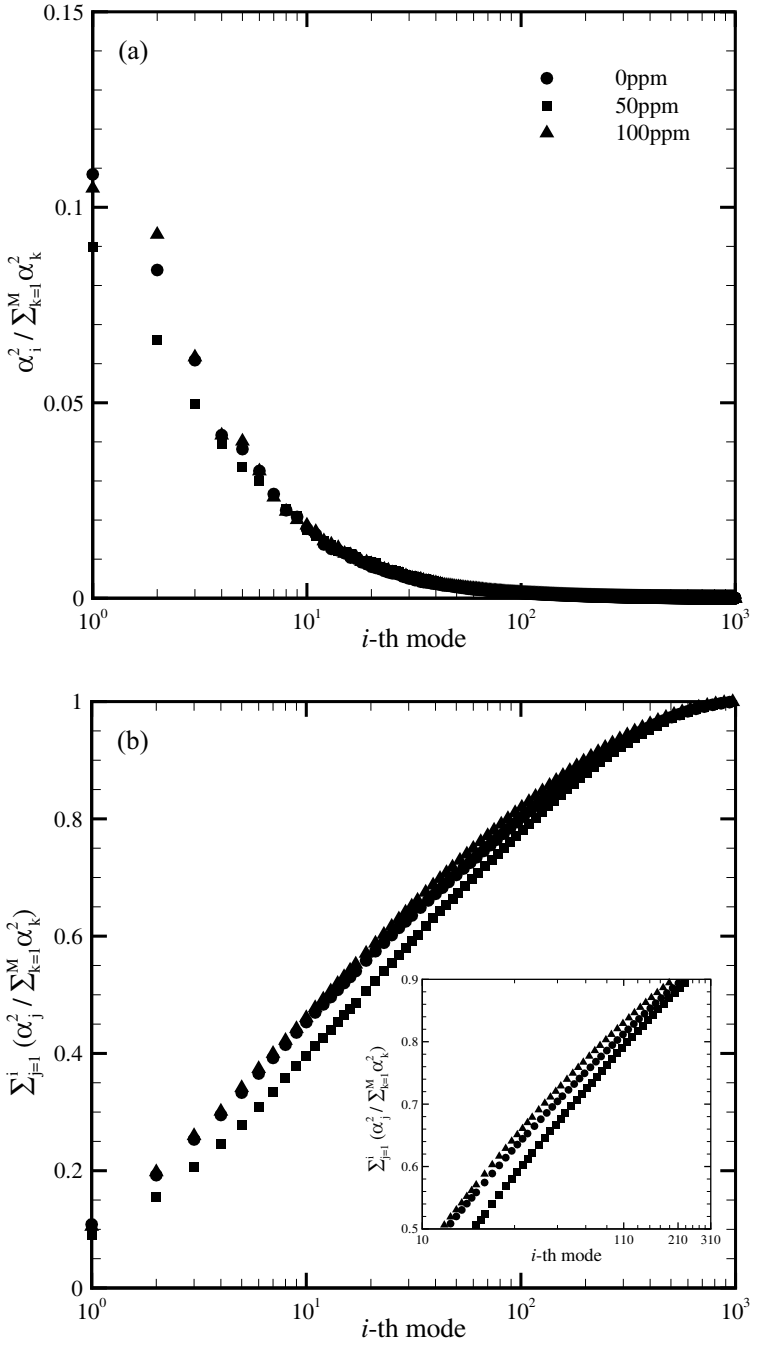

Figure 3.17: a) POD energy spectrum versus mode number and b) cumulative energy distribution for the free-jet region.

plain water and 100 ppm cases. This observation, in concert with the observation that the mixing layer of the 50 ppm jet was thinner and therefore yielded a longer potential core than the other cases, indicates that the large-scale structures that form at the exit of the nozzle develop slower

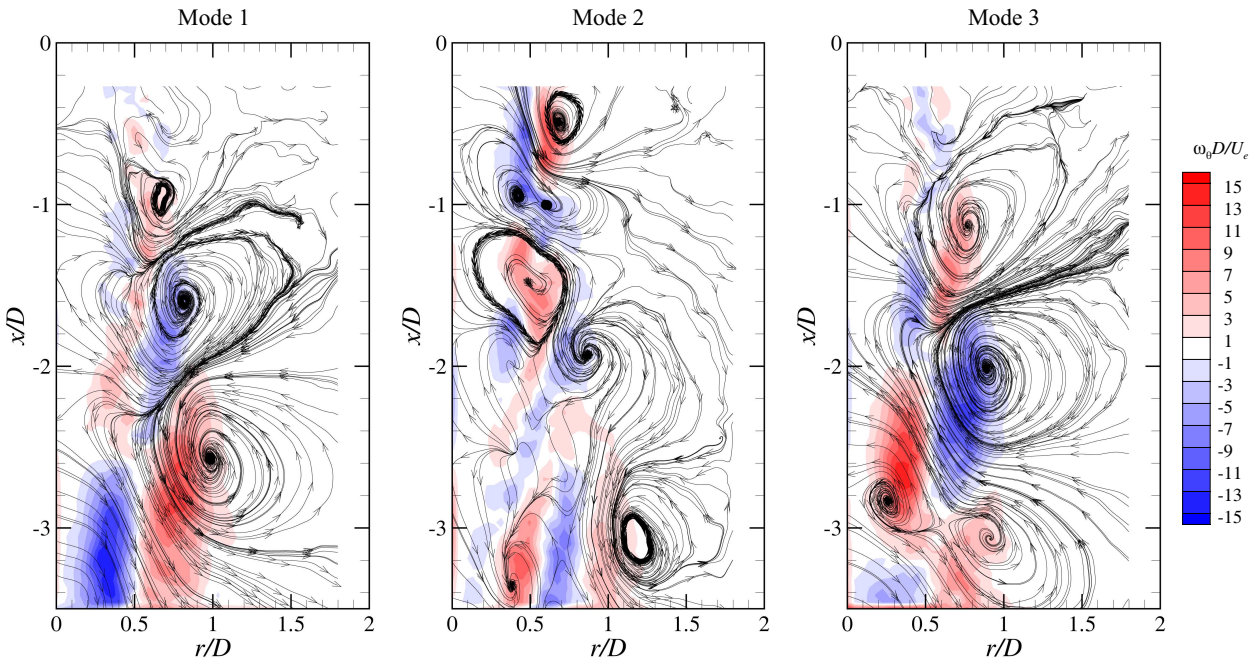

Figure 3.18: Streamline traces overlaid on vorticity contours for the first three POD modes in the free-jet region for plain water (0 ppm).

in the 50 ppm case and thus contain a smaller fraction of the turbulent kinetic energy compared to the other cases. This difference can also be seen in the cumulative energy distribution profiles (figure 3.17b) where it is observed that 13 modes are needed to capture 50% of the TKE in the plain water case while 18 modes are required for the 50 ppm case. With regard to the plain water and 100 ppm cases, smaller differences are noted in the energy content of the large scales as the mode-1 content for water exceeds that of the 100 ppm case while the trend is opposite for the mode-2 content. Nevertheless, there does exist an, albeit small, difference in the cumulative energy distribution between these two cases as the 100 ppm case contains a slightly higher level of TKE for fixed mode number compared to the water case. In particular, 87 modes are required to capture 80% of the TKE for the 100 ppm case compared to 100 for plain water. Again recalling that the mixing layer of the 100 ppm jet thickened more rapidly than the other cases, resulting in a shorter potential core, these trends indicate a higher degree of development and coherence of the largest scales in the 100 ppm jet in the near-nozzle region.

Figures 3.18–3.20 present streamline traces of the three most energetic POD modes in the free-jet region for the plain water, 50 ppm and 100 ppm cases, respectively. Vorticity contours are

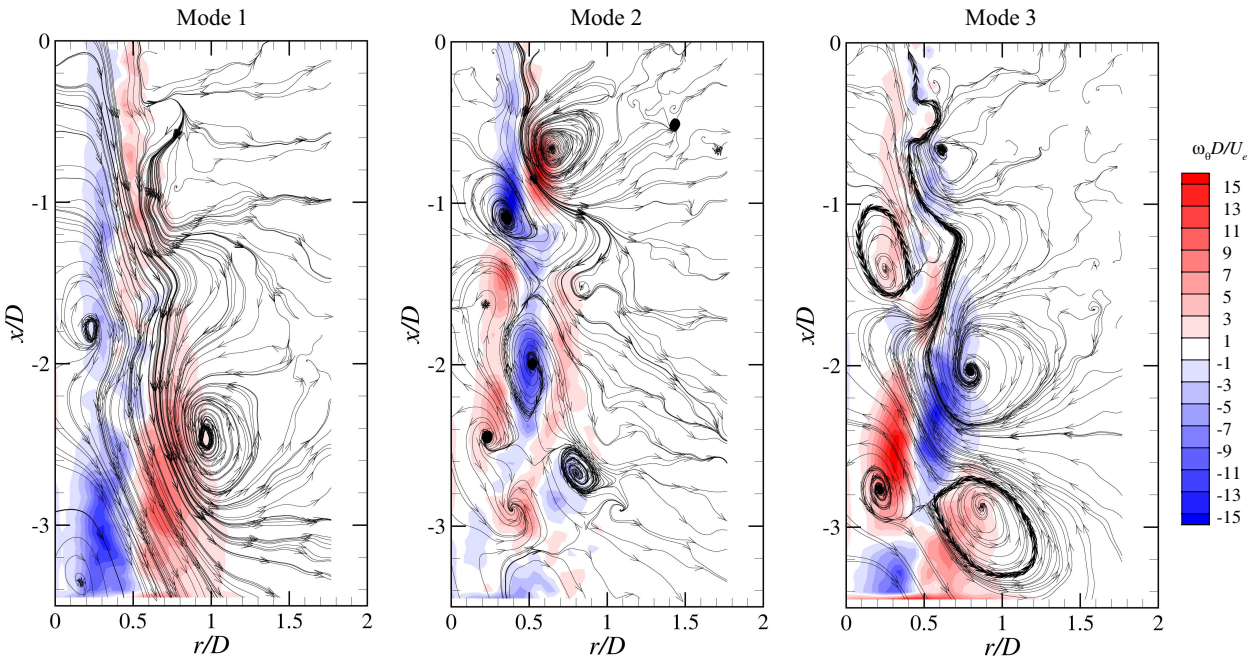

Figure 3.19: Streamline traces overlaid on vorticity contours for the first three POD modes in the free-jet region for the 50 ppm solution.

presented in the background as well. Consistent with the discussion above regarding energy content, the largest scales of the 50 ppm case appears less mature and weaker than those present in the plain water and 100 ppm cases. This observation is consistent with the longer axial distance required to reach the end of the potential core in the 50 ppm jet compared to the other two. This effect is particularly evident when comparing mode 1 for the 50 ppm and 100 ppm jets in figures 3.19 and 3.19, respectively, where less coherence is evident in the 50 ppm case. Similar characteristics are quite evident in mode 3 as well.

3.4.3 Impingement region

Figure 3.21 presents the energy spectra and cumulative energy profiles in the impingement region demarcated in figure 3.16 for the three jets. As in the free-jet region, a redistribution of TKE is noted with the addition of polymer. In particular, the 50 ppm jet contains less TKE in the first few (larger spatial scale) modes compared to the plain water and 100 ppm jets. The slight enhancement of larger-scale TKE content in the 100 ppm jet compared to the plain water case is amplified in the impingement region where the energy content of the first several POD modes for the latter

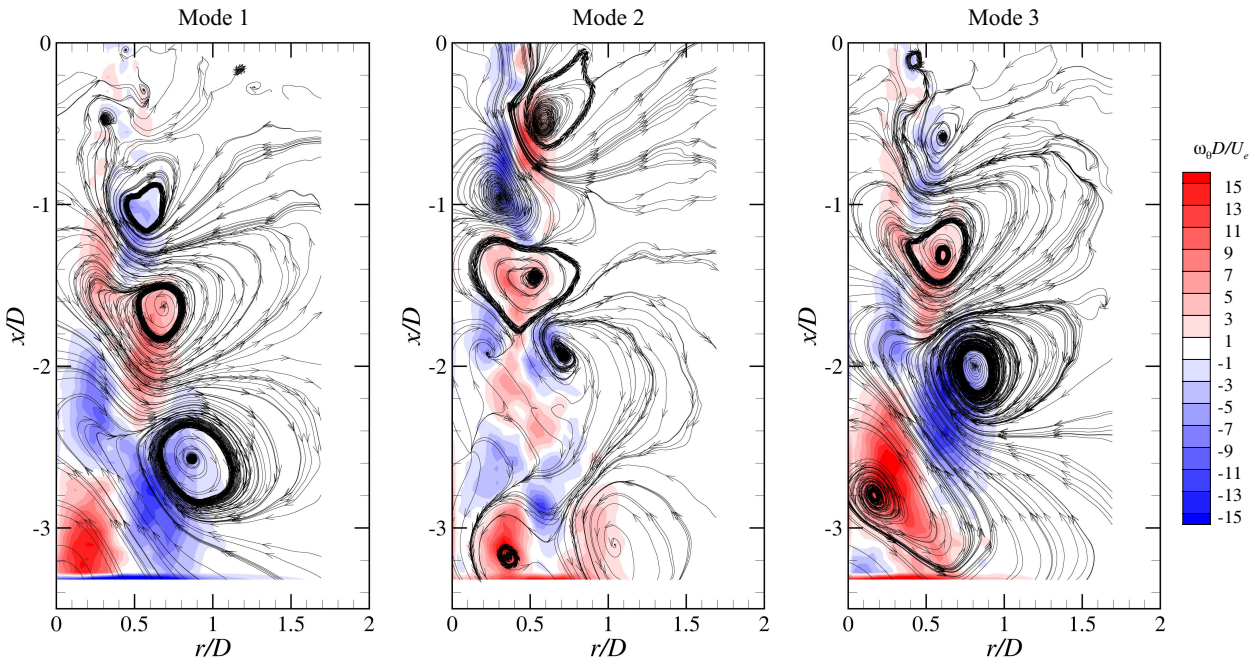

Figure 3.20: Streamline traces overlaid on vorticity contours for the first three POD modes in the free-jet region for the 100 ppm solution.

well-exceed those of the former. This difference is notable in the profiles of cumulative energy as the 100 ppm case sits above the plain water case which in turn sits above the 50 ppm case. Thus, the development of the largest scales of the turbulence in the free-jet region, where this disparity in energy content was first noted, is amplified in the impingement region where these large-scale structures interact with the impingement surface. In this regard, 14 modes are required to capture 50% of the TKE for the plain water case while 17 and 12 modes are needed for the 50 ppm and 100 ppm cases, respectively.

Figures 3.22–3.24 present streamline traces of the three most energetic POD modes in the impingement region for the plain water, 50 ppm and 100 ppm cases, respectively. Consistent with the energy content trends, the 50 ppm case exhibits weaker, less coherent vortical structures compared to the plain water and 100 ppm cases. Mode 1 for these three cases demonstrates this difference quite clearly. Of interest, the two polymer cases show distinct differences to the plain water case in mode 3 where the latter shows a region of closed streamlines and negative vorticity sitting above a region of closed streamlines with positive vorticity. In contrast, the two polymer cases reveal an alteration of this ordering as well as a reduction in the coherence of these motions. Thus, addition

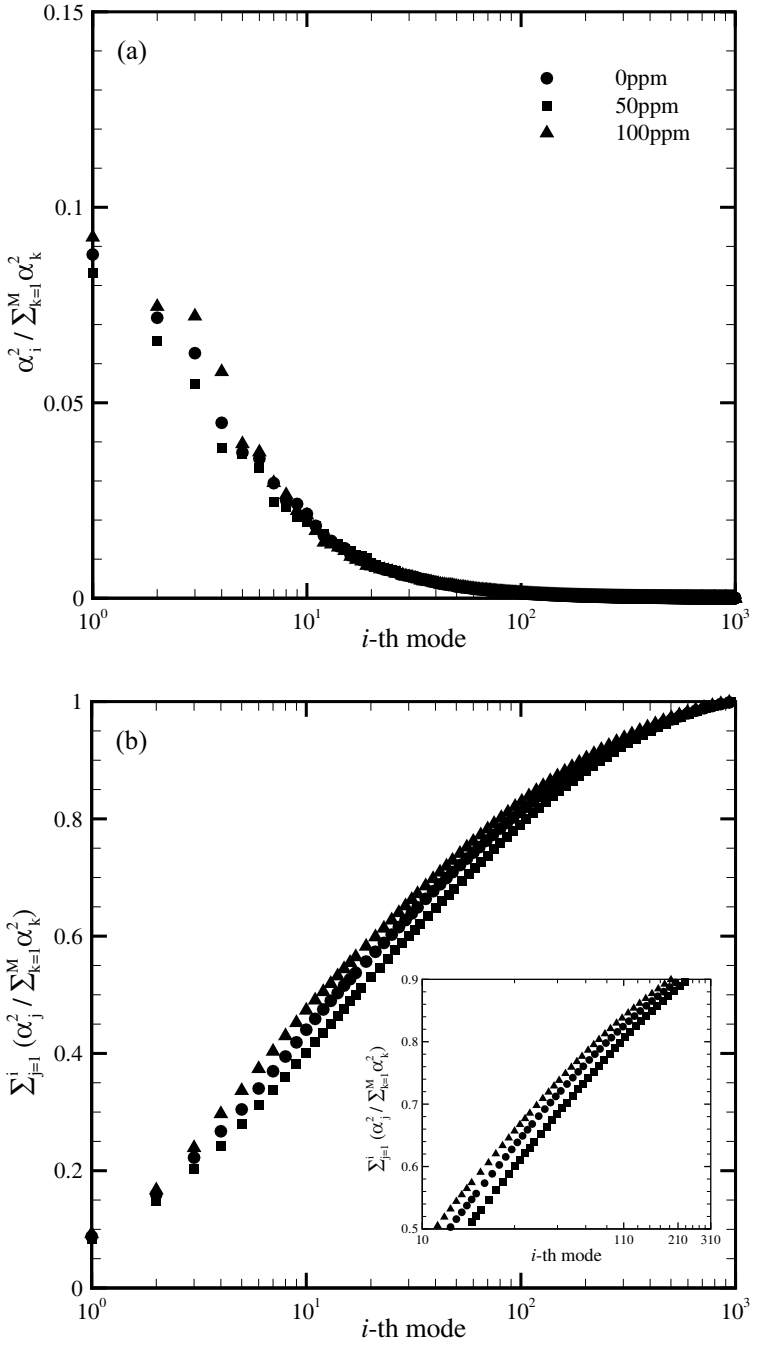

Figure 3.21: a) POD energy spectrum versus mode number and b) cumulative energy distribution for the impingement region.

of polymer does indeed alter the structural interactions at the impingement surface.

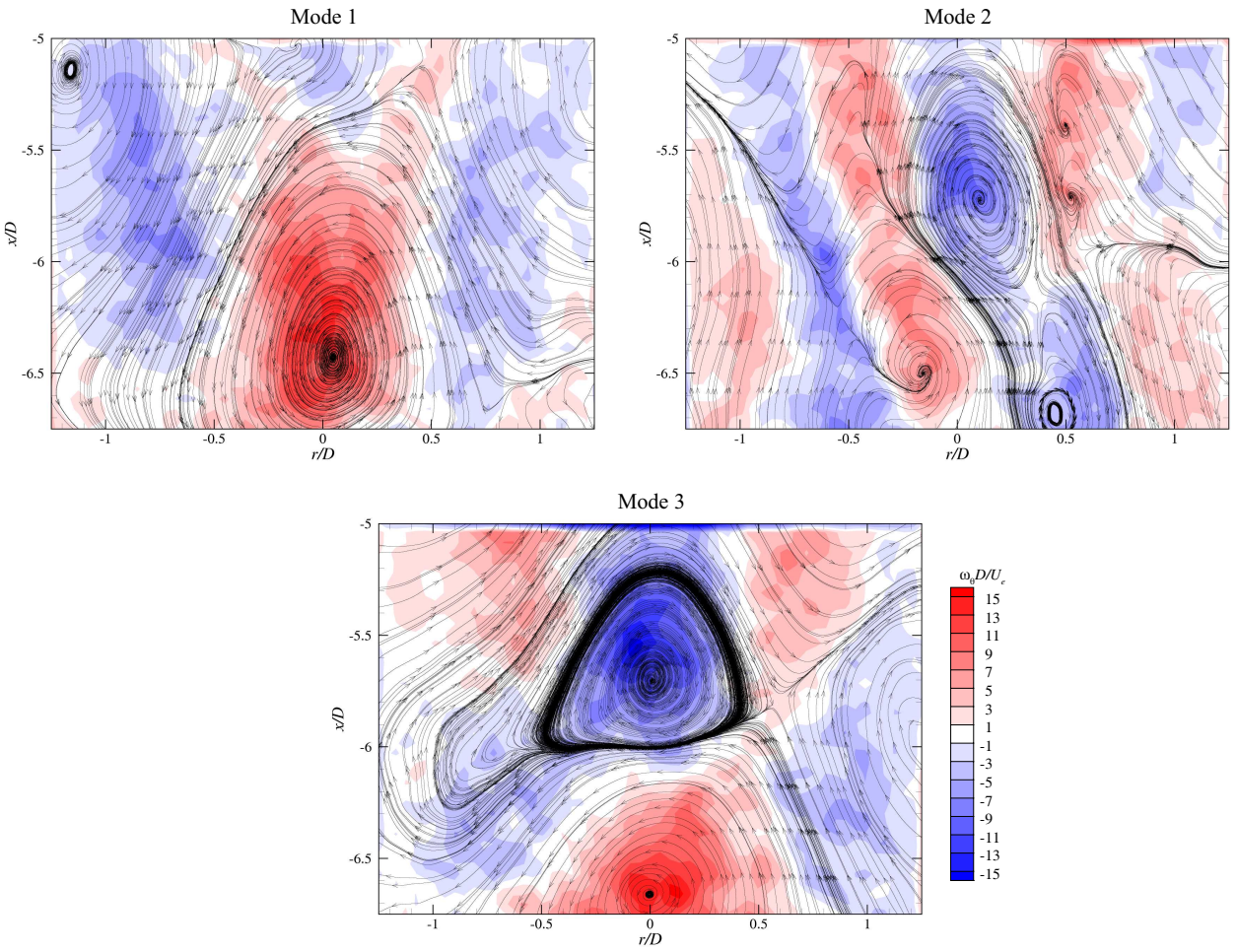

Figure 3.22: Streamline traces overlaid on vorticity contours for the first three POD modes in the impingement region for plain water (0 ppm).

3.4.4 Wall-jet region

Figure 3.25 presents energy spectra and cumulative energy distributions for flow in the wall-jet region for the three jet cases. In contrast to the differences observed in the free-jet and impingement regions, the energy spectra for the three jets show far more consistency apart from mode 1 where slightly more TKE is contained in the 50 ppm case compared to the plain water and 100 ppm jets. The cumulative energy profiles reflect this consistency as all three cases show similar cumulative energy trends. The upper-left inset to figure 3.25b provides a zoomed-in view of the cumulative energy content for the first few POD modes (largest scales) and in this range of mode numbers the polymer cases contain slightly more energy than the plain water case. In contrast, the lower-right

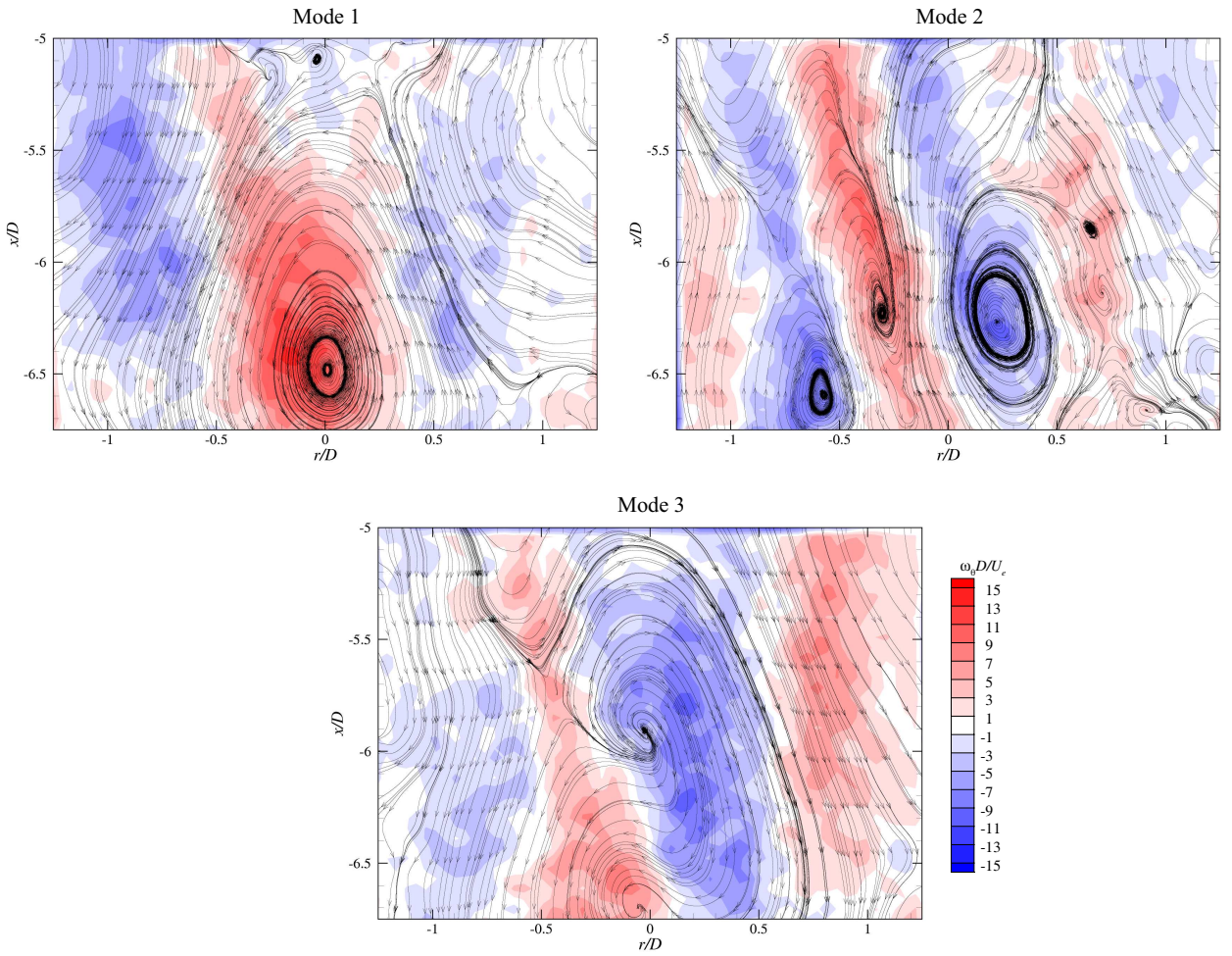

Figure 3.23: Streamline traces overlaid on vorticity contours for the first three POD modes in the impingement region for the 50 ppm solution.

inset, which focuses on modes in the range of 10–17, reveals a slightly higher TKE content for fixed mode number for the plain water case compared to the polymer jets. This latter trend is consistent with the likely onset of drag-reducing behavior in the polymer flows along the impingement surface within the thin boundary-layer under formation, though only a portion of the wall-jet region considered in the POD calculations is turbulent in nature. Thus, this effect is not amplified in the present analysis.

Finally, figures 3.26–3.28 present streamline traces of the three most energetic modes in the wall-jet region for the plain water, 50 ppm and 100 ppm cases, respectively. The modes for the different jets show qualitative consistency as one might expect given the consistency noted in their

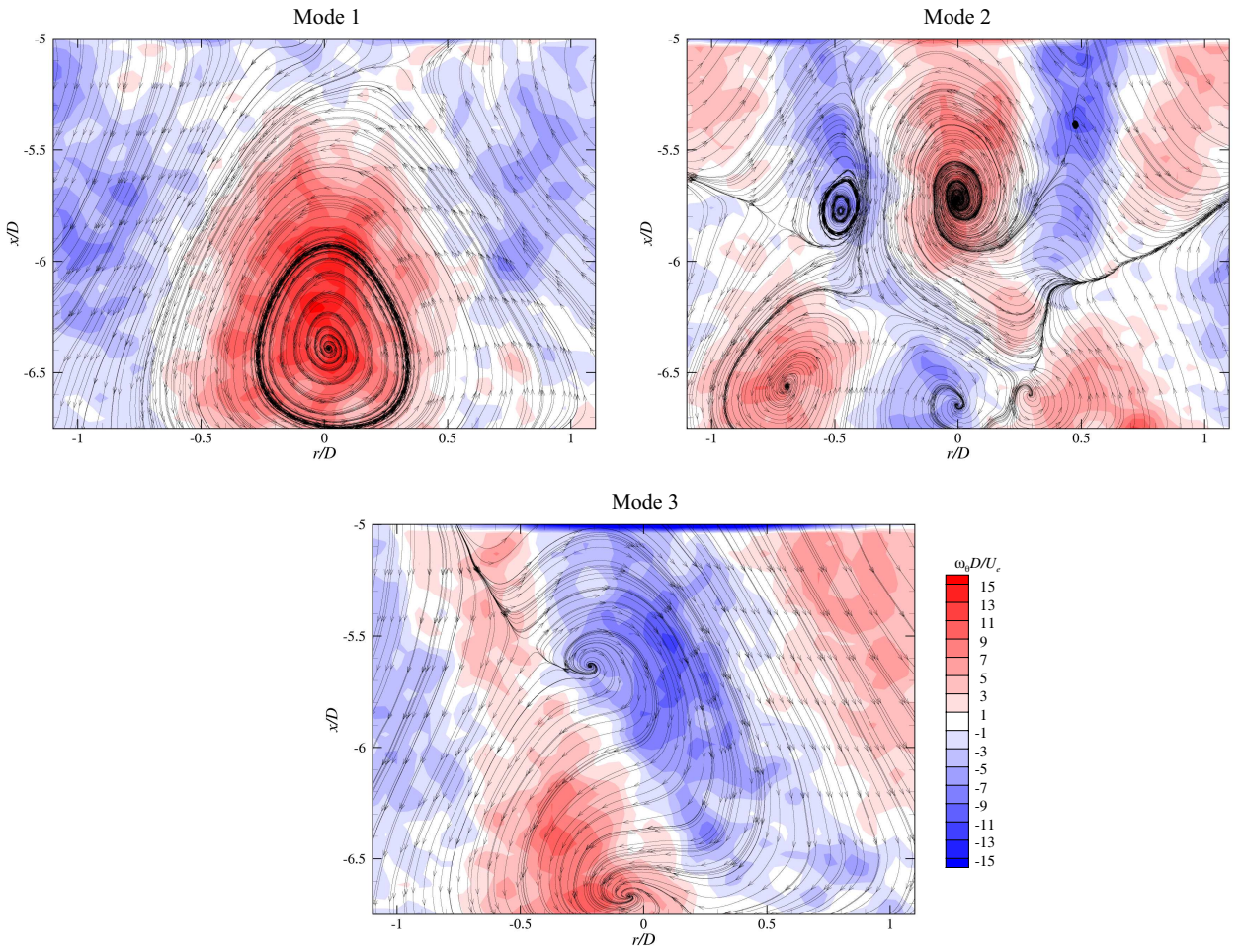

Figure 3.24: Streamline traces overlaid on vorticity contours for the first three POD modes in the impingement region for the 100 ppm solution.

respective energy spectra. However, there is a slight shift in the location of the regions of closed streamlines, with the two polymer cases shifted toward the impingement region relative to the plain water case. In addition, the coherence of these motions appears reduced slightly in the polymer cases, particularly for the 100 ppm jet. This reduction in coherence within the wall jet for the 100 ppm case is again consistent with the possibility of turbulence suppression in this wall-bounded region of the flow.

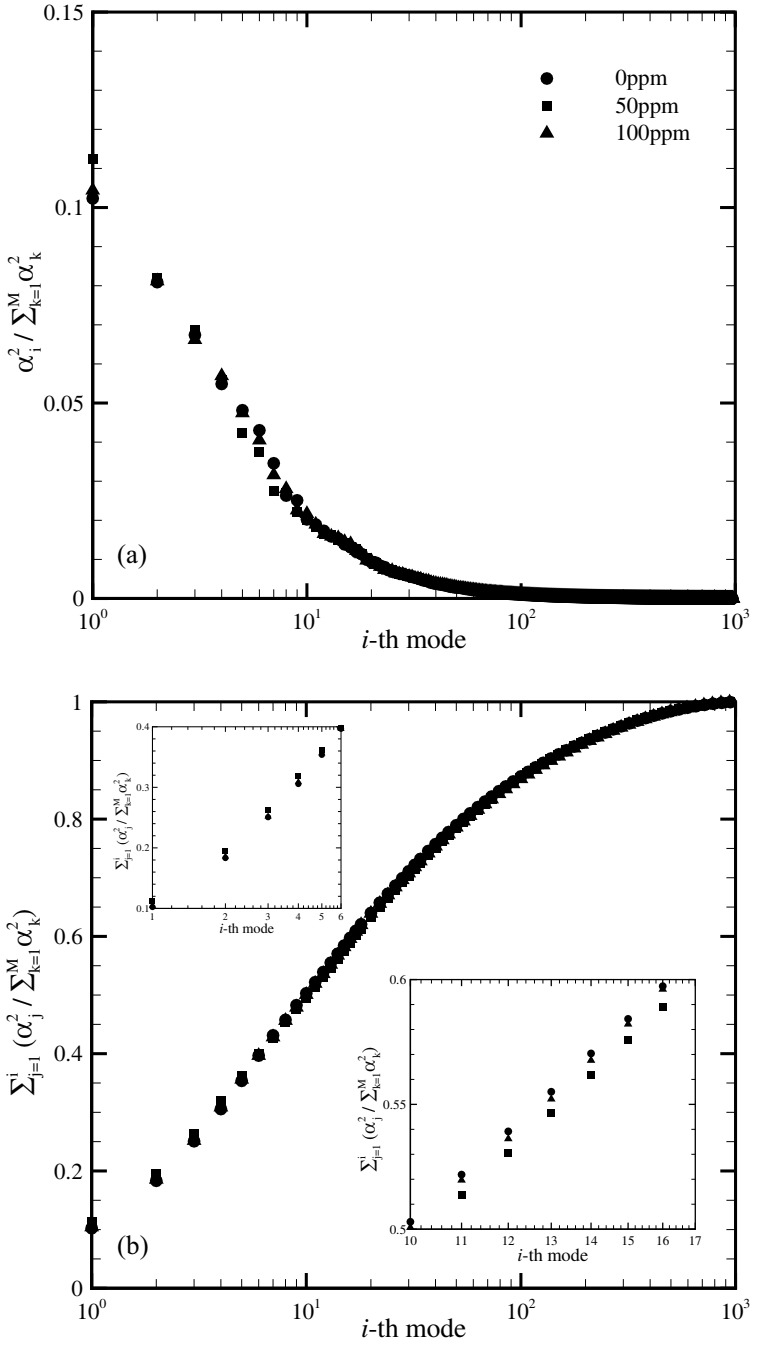

Figure 3.25: a) POD energy spectrum versus mode number and b) cumulative energy distribution for the wall-jet region.

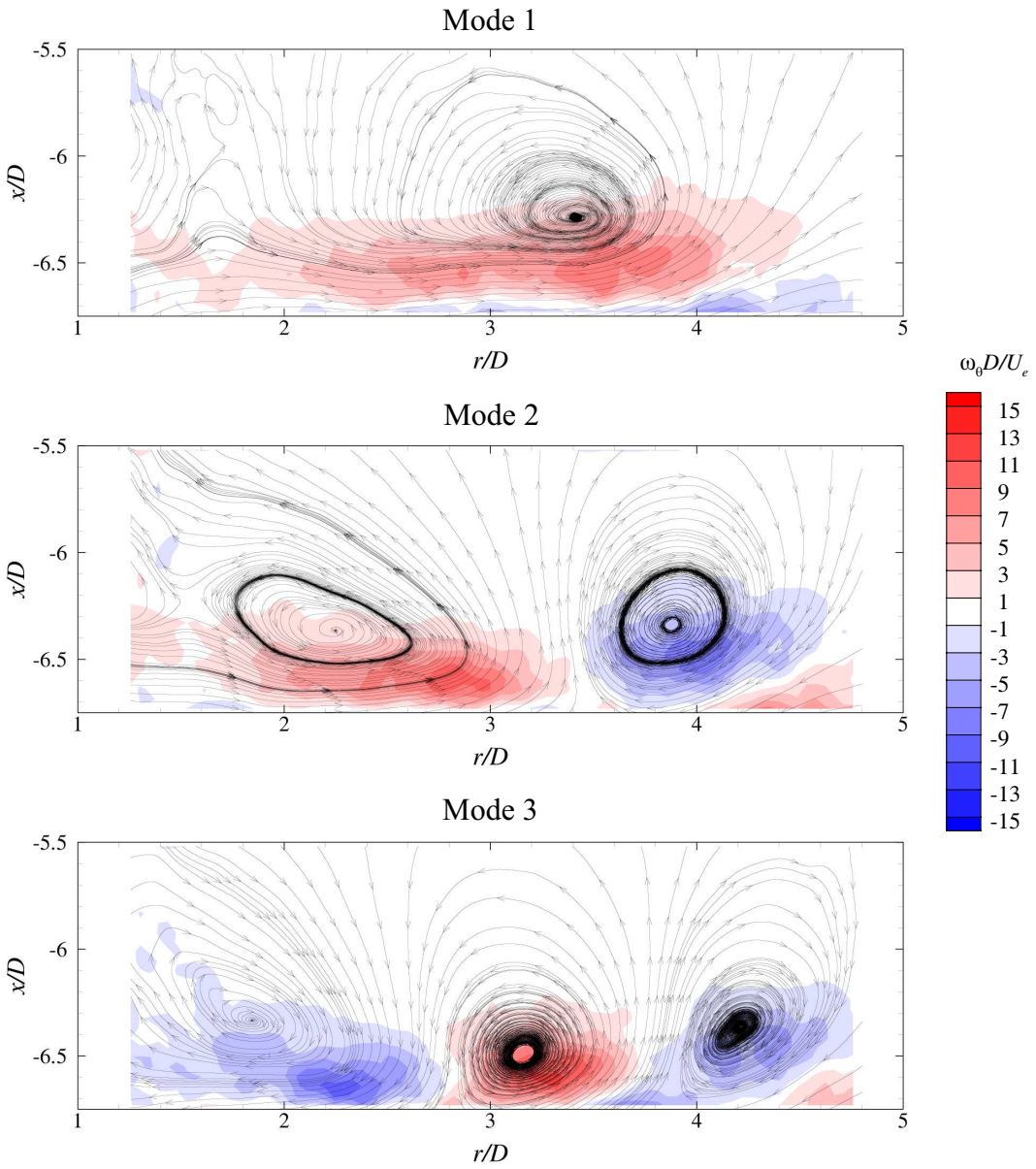

Figure 3.26: Streamline traces overlaid on vorticity contours for the first three POD modes in the wall-jet region for plain water (0 ppm).

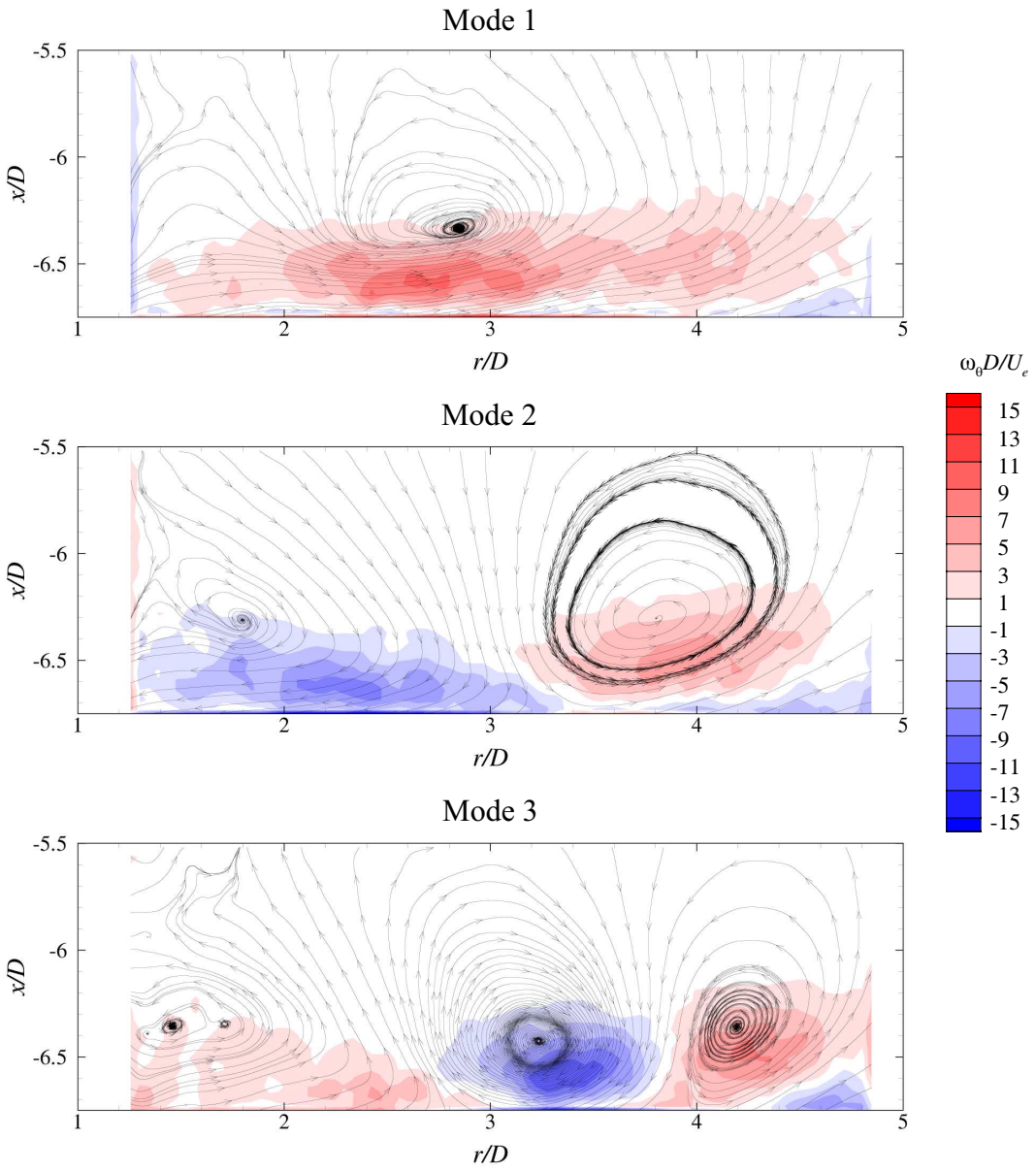

Figure 3.27: Streamline traces overlaid on vorticity contours for the first three POD modes in the wall-jet region for the 50 ppm solution.

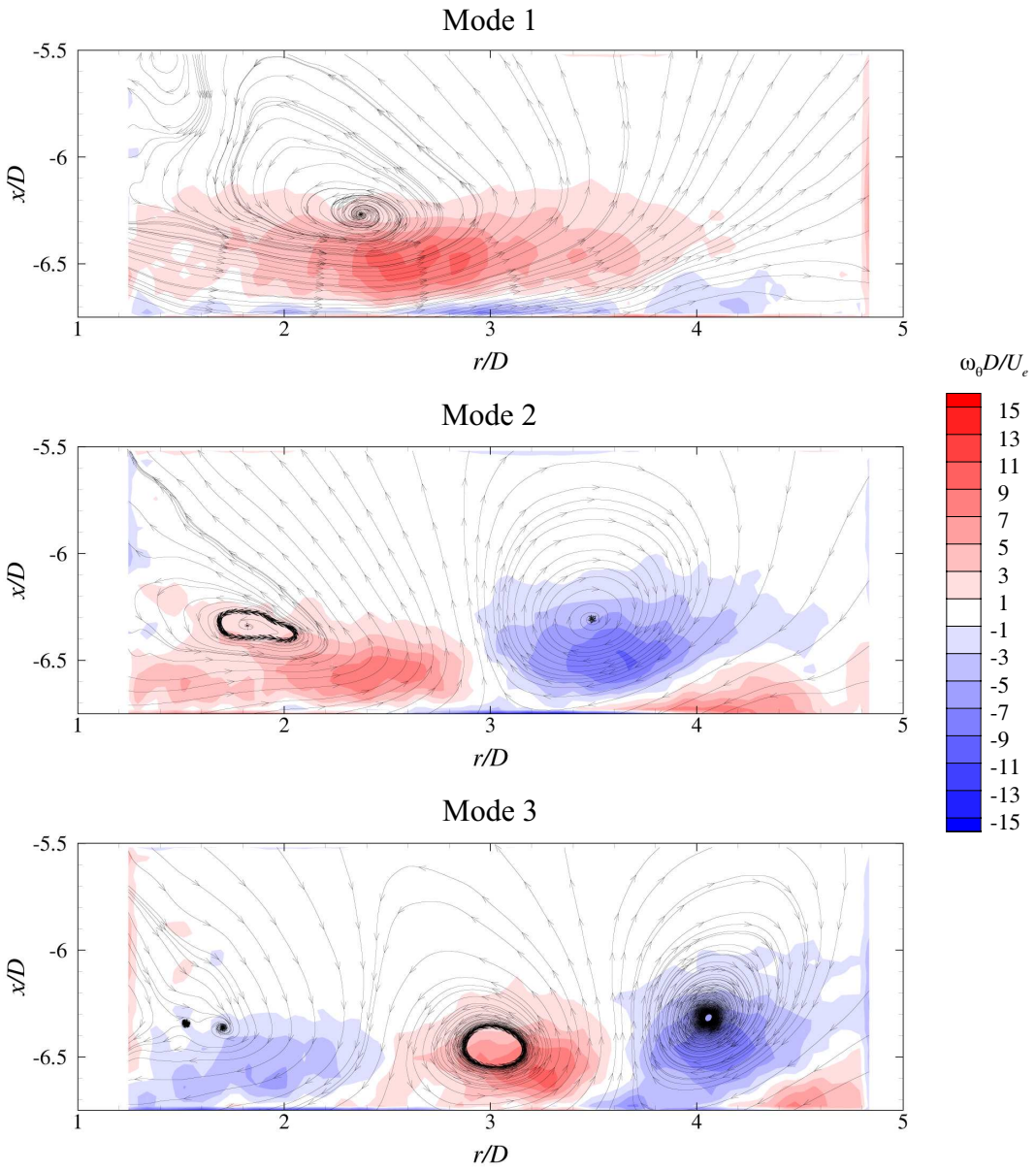

Figure 3.28: Streamline traces overlaid on vorticity contours for the first three POD modes in the wall-jet region for the 100 ppm solution.

Chapter 4

Concluding Remarks and Future Work

The present effort involved the acquisition of 2D-PIV data in the axial–radial ($x - r$) plane of submerged turbulent impinging jets of water and dilute polymer solutions of POLYOX^{TM} WSR-205 at concentrations of 50 ppm and 100 ppm. These measurements were conducted at a nominal Reynolds number of $\mathrm{Re}_D = 23000$ and at a nozzle-to-wall distance of $H/D = 6.8$. From these experiments results, we observed the following behavior:

- Addition of POLYOX^{TM} WSR-205 in submerged axisymmetric turbulent jets induces modifications in their entrainment rates, initial thickness of their mixing layers and may induce viscoelastic effects such as "die-swell" at the exit of the nozzle. For dynamically-similar jets (comparable Reynolds number), depending on the concentration of polymers, these effects combined may either enhance or reduce the spreading rate of the jet which results in a shortening or elongation of the potential core as a consequence. For our case of $\mathrm{Re}_D = 23000$, the onset for enhanced spreading rate (and shortening of the potential core) of the free jet appears to occur in the concentration range $50\,\mathrm{ppm} < c < 100\,\mathrm{ppm}$.

- Both polymer solutions exhibited enhancement in their entrainment rates. However, while the 100 ppm solution presented strong entrainment enhancements in both the free-jet and wall-jet regions, the 50 ppm solution presented a minor enhancement in the free-jet region and a strong enhancement in the wall-jet region. Moreover, the entrainment rate of the 50 ppm solution in the wall jet region was slightly higher than the 100 ppm solution.

- In the free jet region, the 100 ppm solution exhibited a strong enhancement in TKE and both axial- and radial-normal Reynolds stresses, while the 50 ppm solution exhibited some attenuation of the same single-point statistics with respect to the plain water case.

- The wall jet of the 100 ppm solution exhibited some suppression in TKE and Reynolds normal stresses in the interval $1.5 < r/D < 5.4$. On the other hand, the 50 ppm solution showed no significant effects when compared with the plain water case.

- The dynamics of the Reynolds shear stress seemed to be the same for all jets in the free jet region, since all profiles collapse with one-another. This similarity extends to the wall-jet region up to $r/D \approx 5.4$–the distance at which the profile for the 100 ppm solution departs from the others and subsequently decays at a higher rate.

- The near region of the free jet is dominated by the presence and interaction of large-scale coherent structures, namely ring or spiral vortices. The axial extent of the near region coincides with the length of the potential core of the jet, L. This distance is coincident with the distance along which the coherent structures evolve before breaking down in the puffing region. In addition, it was observed that the length of the potential core, and in consequence the axial extent of the near region, depends on the exit conditions of the jet (advected turbulence intensity, velocity profile, mixing-layer thickness and possible viscoelastic effects).

- It was observed that what we term the *enhancement limit* of $H/D \leq 6.0$ proposed for the existence of non-monotonic radial turbulence intensity profiles in the impingement and wall-jet regions (which has been linked to non-monotonic behavior in Nusselt number) does not hold for the present jets with $H/D = 6.8$. In fact, non-monotonic behavior was observed for all three jet cases despite exceeding the accepted nozzle-to-wall distance threshold. In fact, the present results indicate that this threshold might be more appropriately defined in terms of the structure of the free jet. Specifically, the *enhancement limit* would be achieved for nozzle-to-wall distances in the neighborhood of the puffing region. As the potential core is a defining feature of the structure of the near region of a free jet, it would be more convenient to use its length L, instead of the nozzle diameter D, to normalize the axial coordinate of the jet. Based on the present results and regardless of the exit conditions of the jet, a nozzle-to-wall distance of, for instance, $H/L \approx 1.25 - 1.5$, would likely ensure that the impingement region is exposed to the puffing region of the free jet and thus would be within the *enhancement limit*.

- The POD analysis revealed a redistribution of TKE with scale in the free-jet, impingement and wall-jet regions. In particular, the 50 ppm case showed a reduction in the TKE content of the largest turbulence scales in the free-jet region while the 100 ppm jet showed a slight enhancement relative to the plain water jet. This redistribution of TKE amongst the large scales was further exacerbated in the impingement region. In contrast, only slight differences in the TKE content was observed in the wall-jet region. Visualization of the most energetic POD modes indicated a loss of coherence in the large-scale motions with the addition of polymer for the 50 ppm case but a slightly enhanced coherence in the 100 ppm case.

With regard to logical future steps toward improving our understanding of this problem, the present results provide significant insight into the complex flow behavior both in the free-jet, impingement and wall-jet regions. From this analysis, it can be conjectured that turbulence enhancement via addition of polymer would enhance the complex vortex interactions that occur in the impingement zone and thus provide a means of enhancing local convective heat transfer in this flow configuration. However, direct *and* simultaneous measurements of both velocity and temperature in the impingement region would provide a direct measure of this enhancement. Specifically, measurements could be made for a heated impingement surface under constant heat flux conditions and the fluid velocity and temperature fields could be simultaneously measured along the axial–radial plane using combined PIV and laser-induced fluorescent thermometry. The latter method uses the temperature-dependence of the fluorescent emission of organic dyes to infer fluid temperature over a measurement plane defined by a laser light-sheet. These simultaneous measurements would provide a means of quantifying local convective heat transfer near the impingement surface as well as way of quantifying the linkage between vortical structures and this enhancement.

In addition, it would be advantageous to study the effect of polymer concentration as well as molecular weight in more detail. It is well-established in wall-bounded flows that such variables play a crucial role in the degree of drag-reduction noted when ppm of polymer are added to a wall-bounded flow. As the present flow configuration contains a significant interaction between the free jet and a surface (as well as the development of a wall jet after impingement), it is likely that concentration and/or molecular weight might play an important role in the turbulence modifications observed in the impingement region.

References

R. J. Adrian, K. T. Christensen, and Z.-C. Liu. Analysis and interpretation of instantaneous turbulent velocity fields. *Experiments in Fluids*, 29:275–290, 2000.

M. Angioletti, R.M. Di Tommaso, E. Nino, and G. Ruocco. Simultaneous visualization of flow field and evaluation of local heat transfer by transitional impinging jets. *International Journal of Heat and Mass Transfer*, 46:1703–1713, 2003.

N. Aubry. On the hidden beauty of the proper orthogonal decomposition. *Theoretical and Computational Fluid Dynamics*, 2(5):339–352, 1991.

N. Aubry, R. Guyonnet, and R. Lima. Spatiotemporal analysis of complex signals: Theory and applications. *Journal of Statistical Physics*, 64(3/4):683–739, 1991.

S.J. Barker. Laser-Doppler measurements on a round turbulent jet in dilute polymer solutions. *Journal of Fluid Mechanics*, 60(4):721–731, 1973.

J.W. Baughn and S. Shimizu. Heat transfer measurements from a surface with uniform heat flux and an impinging jet. *Journal of Heat Transfer; Transactions of the ASME*, 111:1096 – 1098, 1989.

N.S. Berman and H. Tan. Two-component laser Doppler velocimeter studies of submerged jets of dilute polymer solutions. *AIChE Journal*, 31(2):208–215, 1985.

R.B. Bird, R.C. Armstrong, and O. Hassager. *Dynamics of polymeric liquids*, volume 1. Wiley-Interscience, 2nd edition, 1987.

F.K. Browand and J. Laufer. The role of large scale structures in the initial development of circular jets. In *Turbulence in Liquids; proceedings of the 4^{th} biennial symposium on turbulence in liquids*, pages 333–344, Department of Chemical Engineering, University of Missouri–Rolla, 1977. Science Press, Princeton–New Jersey.

W. Cazemier, R. W. C. P. Verstappen, and A. E. P. Veldman. Proper orthogonal decomposition and low-dimensional models for driven cavity flows. *Phys. Fluids*, 10:1685, 1998.

A. Chatterjee. An introduction to the proper orthogonal decomposition. *Current science*, 78(7): 808–817, 2000.

A. Chatterjee, S. C. Dhingra, and S. S. Kapur. Laminar impinging jet heat transfer with a purely viscous inelastic fluid. *Numerical Heat Transfer*, 42:193–213, 2002.

J.H. Citriniti and W.K. George. Reconstruction of the global velocity field in the axisymmetric mixing layer utilizing the proper orthogonal decomposition. *Journal of Fluid Mechanics*, 418: 137–166, 2000.

D. Cooper, D.C. Jackson, B.E. Launder, and G.X. Liao. Impinging jet studies for turbulence model assessment – I. Flow-field experiments. *International Journal of Heat and Mass Transfer*, 36(10): 2675–2684, 1993.

S. Corrsin. Investigation of flow in an axially symmetrical heated jet of air. Technical Report WR–94, NACA, 1943.

S. Corrsin and A.L. Kistler. Free-stream boundaries of turbulent flows. Technical Report 1244, NACA, 1955.

C. R. Doering. The 3D Navier-Stokes problem. *Annual Review of Fluid Mechanics*, 41:109–128, 2009.

N. Dunford and J. T. Schwartz. *Linear Operators, Part II: Spectral Theory (self adjoint operators in Hilbert Space)*. Wiley–Interscience, 1988.

B. P. Epps and A. H. Techet. An error threshold criterion for singular value decomposition modes extracted from PIV data. *Experiments in Fluids*, 38(2):1–13, 2009.

M. Fairweather and G.K. Hargrave. Experimental investigation of an axisymmetric, impinging turbulent jet. 1. Velocity field. *Experiments in Fluids*, 33:464–471, 2002.

J.A. Fitzgerald and S.V. Garimella. A study of the flow field of a confined and submerged impinging jet. *International Journal of Heat and Mass Transfer*, 41(8 – 9):1025 – 1034, 1998.

B. Ganapathisubramani, E.K. Longmire, and I. Marusic. Investigation of three dimensionality in the near field of a round jet using stereo piv. *Journal of Turbulence*, 3:016, 2002.

R. Gardon and J.C. Akfirat. The role of turbulence in determining the heat-transfer characteristics of impinging jets. *International Journal of Heat and Mass Transfer*, 8:1261 – 1272, 1965.

R. Gardon and J. Cobonpue. Heat transfer between a flat plate and jets of air impinging on it. In *International Developments in Heat Transfer; proceedings of the International Heat Transfer Conference*, pages 454–460. ASME–New York, 1962.

P. Glowacki. Turbulence characteristics of impinging jets near the deflecting surface. the effect of polymer additives. *Journal of Non-newtonian Fluid Mechanics*, 33:25–38, 1989.

R. J. Goldstein and M. E. Franchett. Heat transfer from a flat surface to an oblique impinging jet. *J. Heat Transfer*, 110:84–90, 1988.

D.P. Hart. Piv error correction. *Experiments in Fluids*, 29:13–22, 2000.

J. K. Harvey and F. J. Perry. Flow field produced by trailing vortices in the vicinity of the ground. *AIAA J.*, 9:1659–1660, 1971.

P. Holmes, J. L. Lumley, and G. Berkooz. *Turbulence, coherent structures, dynamical systems and symmetry*. Cambridge Monographs on Mechanics. Cambridge, 1996.

J.W. Hoyt and J.J. Taylor. Effect of nozzle shape and polymer additives on water jet appearance. *Transactions of the ASME. Journal of Fluids Engineering*, 101:304–308, 1979.

J.W. Hoyt, J.J. Taylor, and C.D. Runge. The structure of jets of water and polymer solution in air. *Journal of Fluid Mechanics*, 63(4):635–640, 1974.

A.K.M.F. Hussain and V. Ramjee. Effects of the axisymmetric contraction shape on incompressible turbulent flow. *Journal of Fluids Engineering; Tansactions of the ASME*, pages 58 – 69, 1976.

K. Jambunathan, E. Lai, M.A. Moss, and B.L. Button. A review of heat transfer data for single circular jet impingement. *International Journal of Heat and Fluid Flow*, 13(2):106 – 115, june 1992.

S.P. Kezios. *Heat transfer in the flow of a cylindrical air jet normal to an infinite plane.* PhD thesis, Illinois Institute of Technology, 1956.

K. Koziol and P. Glowacki. Turbulent jets of dilute polymer solutions. *Journal of Non-Newtonian Fluid Mechanics*, 32:311–328, 1989.

C. C. Landreth and R. J. Adrian. Impingement of a low reynolds number turbulent circular jet onto a flat plate at normal incidence. *Experiments in Fluids*, 9:74–84, 1990.

R.G. Larson. *The structure and Rheology of complex fluids.* Oxford University Press, 1998.

E.J. List. Turbulent jets and plumes. *Annual Review of Fluid Mechanics*, 14:189 – 212, 1982.

S. Maurel and C. Solliec. A turbulent plane jet impinging nearby and far from a flat plate. *Experiments in Fluids*, 31:687–696, 2001.

A. J. Muller, A. E. Saez, and J. A. Odell. Turbulence suppresion by polymer solutions in opposed jet flows. *AIChE J.*, 41(5):1333–1336, 1995.

C. O. Popiel and L. Boguslawski. Effect of flow structure on the heat and mass transfer on a flat plate in an impinging round jet. In 2^{nd} *UK National Conf. on Heat Transfer*, pages 663–685, 1988.

J. Rohaly, F. Frigerio, and D.P. Hart. Reverse hierarchical piv processing. *Meas. Sci. Technol.*, 13: 984–996, 2002.

J. Sakakibara, K. Hishida, and M. Maeda. Vortex structure and heat transfer in the stagnation region of an impinging plane jet. *Int. J. Heat Mass Transfer*, 40(13):3163–3176, 1996.

E. U. Schlunder and V. Gnielinski. Heat and mass transfer between surface and impinging jets. *Chem. Ing. Tech.*, 39:578–584, 1967.

L. Sirovich. Turbulence and the dynamics of coherent structures. i- coherent structures. ii- symmetries and transformations. iii- dynamics and scaling. *Quarterly of applied mathematics*, 45(3): 561–590, 1987.

K.R. Sreenivasan and C.M. White. The onset of drag reduction by dilute polymer additives, and the maximum drag reduction asymptote. *Journal of Fluid Mechanics*, 409:149–164, 2000.

H. Usui and Y. Sano. Turbulence structure of submerged jets of dilute polymer solutions. *J. Chem. Eng. Japan*, 13:401, 1980.

P.S. Virk. Drag reduction fundamentals. *AIChE Journal*, 21(4):625–656, 1975.

S.A. Vlasov, V.N. Kalashnikov, B.F. Mulchenko, B.S. Rinkevichyus, and V.I. Smirnov. The long-range nature of turbulent submerged jets of polymer solutions. *Fluid Mechanics–Soviet Research*, 2(1):108–111, January-February 1973.

J. D. A. Walker, C. R. Smith, A. W. Cerra, and T. L. Doligalski. The impact of a vortex ring on a wall. *Journal of Fluid Mechanics*, 181:99–140, 1987.

Y. Wu and K. T. Christensen. Population trends of spanwise vortices in wall turbulence. *Journal of Fluid Mechanics*, 568:55–76, 2006.

J. Zhou, R. J. Adrian, S. Balachandar, and T. M. Kendall. Mechanisms for generating coherent packets of hairpin vortices in channel flow. *Journal of Fluid Mechanics*, 387:353–396, 1999.